[Published as *Journal of the Optical Society of America, A* (11)3050–3068, 1994.]

Gradient and Curvature from Photometric Stereo Including Local Confidence Estimation

Robert J. Woodham

Laboratory for Computational Intelligence
University of British Columbia
Vancouver, BC, Canada
V6T 1Z4

tel: (604) 822-4368
fax: (604) 822-5485
email: woodham@cs.ubc.ca

Abstract

Photometric stereo is one technique for 3D shape determination that has been implemented in a variety of experimental settings and that has produced consistently good results. The idea is to use intensity values recorded from multiple images obtained from the same viewpoint but under different conditions of illumination. The resulting radiometric constraint makes it possible to obtain local estimates of both surface orientation and surface curvature without requiring global smoothness assumptions and without requiring prior image segmentation.

This paper moves photometric stereo one step closer to practical viability by describing an experimental setting in which surface gradient estimation is achieved on full frame video data at near video frame rates (i.e., 15Hz). The implementation uses commercially available hardware. Reflectance is modeled empirically using measurements obtained from a calibration sphere. Estimation of the gradient, (p, q), requires only simple table lookup. Curvature estimation uses, in addition, the reflectance map, $R(p, q)$. The required lookup table and reflectance maps are derived during calibration. Because reflectance is modeled empirically, no prior physical model of the reflectance characteristics of the objects to be analyzed is assumed. At the same time, if a good physical model is available, it can be retrofit to the method for implementation purposes.

Photometric stereo is subject to error in the presence of cast shadows and interreflection. No purely local technique can succeed since these phenomena are inherently non-local. Nevertheless, this paper demonstrates that one can exploit the redundancy in three light source photometric stereo to, in most cases, locally detect the presence of cast shadows and interreflection. Detection is facilitated by explicitly including a local confidence estimate in the lookup table used for gradient estimation.

1 Introduction

The purpose of computational vision is to produce descriptions of a 3D world from 2D images of that world, sufficient to carry out a specified task. Robustness in many tasks is improved when use is made of all the information available in an image, not just that obtained from a sparse set of features. The idea of using multiple images obtained from the same viewpoint but under different conditions of illumination has emerged as a principled way to obtain additional local radiometric constraint in the computation of shape-from-shading. In many cases, multiple images overdetermine the solution locally. This further improves robustness by allowing local validation of the radiometric model used.

Photometric stereo is one technique for shape-from-shading that has been implemented in a variety of experimental settings and that has produced consistently good results. The underlying theory follows from principles of optics. An image irradiance equation is developed to determine image irradiance as a function of surface orientation. This equation cannot be inverted locally since image brightness provides only one measurement while surface orientation has two degrees of freedom. Brightness values obtained from the same viewpoint but under different conditions of illumination do make it possible to obtain dense, local estimates of both surface orientation and surface curvature, without requiring global smoothness assumptions and without requiring prior image segmentation. In three light source photometric stereo, the three local intensity measurements overdetermine the two degrees of freedom of surface orientation. Similarly, the six local spatial derivatives of intensity overdetermine the three degrees of freedom of surface curvature. Photometric stereo was originally described in [1, 2]. The first implementation was by Silver [3]. Photometric stereo has since been used for a variety of recognition and localization tasks [4, 5, 6, 7, 8, 9]. The relation to surface curvature also has been explored [10, 11, 12, 13, 14, 15].

Optics determines that an image irradiance equation necessarily exists but says very little about the particular form that image irradiance equation must take. Of course, one can exploit situations where the reflectance properties of a material are known to satisfy a particular functional form. Formal analysis of these situations helps to establish the existence, uniqueness and robustness of solution methods under varying degrees of uncertainty and approximation. Implementation also is facilitated because the resulting computations typically involve equations of known form with unknown coefficients that can be determined as a problem of parameter estimation. By now, the literature on reflectance models applicable to computer graphics and computer vision is quite vast. Some examples are explicit to photometric stereo [16, 17, 18, 19].

The usual formulation of an image irradiance equation assumes that each surface element only receives illumination directly from the light source(s). This is correct for scenes consisting of a single convex object. In general, a surface element also receives illumination indirectly from light reflected from other surface elements in the scene. Interreflection is important for two reasons. First, as demonstrated by Gilchrist [20], interreflection near concave junctions is perceptually salient. It is determined by the intrinsic reflectance (i.e., albedo) of the surface material, independent of the amplitude of the ambient illumination [21, 22]. Second, local shape recovery methods are unreliable if interreflection is not taken into account, as recently has been shown [23, 24].

Indeed, photometric stereo is subject to error in the presence of cast shadows and interreflection. No purely local technique can succeed since these phenomena are inherently non-local. Nevertheless, this paper demonstrates that one can exploit the redundancy in three light source photometric stereo to, in most cases, locally detect the presence of cast shadows and interreflection. Detection is facilitated by explicitly including a local confidence estimate in the lookup table used for gradient estimation.

Here, it is assumed that objects to be analyzed are made of a single material. Reflectance properties are measured using a calibration sphere made of that material. Measurements from the calibration sphere are directly applicable to the analysis of other objects of different shape but made of the same material and illuminated and viewed under the same conditions. In this way, a material with any reflectance characteristic can be handled, provided that the necessary calibration can be done. In some applications, it may be necessary to use paint (or other coating) to match reflectance properties between a calibration sphere and the objects to be analyzed.

Three representations for reflectance data are employed. First, the relationship between measured intensity and surface gradient is represented by the familiar reflectance map, $R(p,q)$. Second, for a material with constant albedo, triples of measured intensity values, $[E_1, E_2, E_3]$, are shown to define a 2D surface in the 3D coordinate space whose axes are E_1, E_2 and E_3. In the absence of interreflection and cast shadows, all triples of measured intensity fall on this surface. Interreflection causes some intensity values to be larger than expected. Cast shadows cause some intensity values to be smaller than expected. Thus, in practice, not all measured triples will lie exactly on the specified surface. Third, the relationship between triples of intensity values, $[E_1, E_2, E_3]$, and surface gradient is represented in a lookup table for implementation purposes.

In the implementation described, each measured triple is projected onto the 2D calibration surface in order to estimate the gradient. The distance each measured triple needs to be projected is used to define a local confidence estimate. Projection tends to decrease error due to interreflection. Of course, any claim to quantitative correction would be fortuitous since neither interreflection nor cast shadows are a local effect. On the other hand, the local confidence estimate is a reliable way to notice when a measured triple does not lie on the required surface. This supports the local detection of interreflection and cast shadows. Experimental measurements verify that this is indeed the case. Local detection of interreflection can be used to prevent erroneous surface reconstruction in regions so detected. Should accurate surface reconstruction be the goal, this becomes useful input to schemes intended to reason more globally, such as the one described in [24].

This paper moves photometric stereo closer to practical viability in two ways. First, an experimental setting is described in which the multiple images required for photometric are acquired simultaneously at video rates. No light sources need to be turned on and off. Instead, spectral multiplexing is used. Three spectrally distinct light sources illuminate the work space from different directions and a suitable RGB color camera acquires three-channel video images that subsequently are treated as three separate B&W images, one corresponding to each condition of illumination. Second, commercially available image processing hardware is used to pass the three-channel video data through a lookup table of length 2^{18}. Lookup table output includes both the gradient and the local confidence estimate. Overall, processing of full frame video data occurs at near video frame rates (i.e., 15Hz).

Section 2 provides the background and theory. Section 3 describes the particular implementation and reports on the experiments performed. Section 4 provides a brief discussion and summary of the conclusions following from the work reported. Finally, Appendix A derives the results cited in Section 2 that are unique to the Lambertian case.

2 Background and Theory

A given spatial arrangement of objects, made of a given set of materials, illuminated in a given way, and viewed from a given vantage point, determine an image according to the laws of optics. Geometric equations determine where each point on a visible surface appears in the image and corresponding radiometric equations determine its brightness and color.

Reflectance modeling is difficult, in general, because complexities arise at several levels. Local reflectance depends not only on the intrinsic optical properties of a material but also, for example, on its surface roughness. Geometric ray analysis of surface microstructure can be complex. At finer scales, one also needs to take into account the wave nature of light, adding even more complexity. In scenes consisting of multiple objects, geometric analysis at the macroscale also becomes complex, making it difficult to deal effectively with interreflections and cast shadows. Despite this, there is considerable work on reflectance models for computer vision. The edited collection [25] provides a good introduction to the relevant literature.

A key observation, first made by Horn [21], is that image irradiance can be written as a function only of surface orientation, for many imaging situations of practical importance. Horn's work, formulated for the problem of shape from shading, introduced the idea of the reflectance map. Reflectance maps can be derived from formal reflectance models, when they are available, or, as is the case here, when they can be measured empirically.

2.1 Shape from Shading and the Reflectance Map

The standard geometry of shape from shading is assumed. That is, let the object surface be given explicitly by $z = f(x, y)$ in a left-handed Euclidean coordinate system, where the viewer is looking in the positive Z direction, image projection is orthographic, and the image XY axes coincide with the object XY axes. The surface *gradient*, (p, q), is defined by

$$p = \frac{\partial f(x,y)}{\partial x} \quad \text{and} \quad q = \frac{\partial f(x,y)}{\partial y}$$

so that a surface normal vector is $[p, q, -1]$. Thus, the gradient, (p, q), is one way to represent surface orientation. An image irradiance equation can be written as

$$E(x,y) = R(p,q) \tag{1}$$

where $E(x, y)$ is the image irradiance and $R(p, q)$ is called the *reflectance map*. A reflectance map combines information about surface material, scene illumination and viewing geometry into a single representation that determines image brightness as a function of surface orientation.

Given an image, $E(x, y)$, and the corresponding reflectance map, $R(p, q)$, shape from shading typically is defined to be the problem of determining a smooth surface, $z = f(x, y)$, that satisfies the image irradiance equation over some domain, Ω, including any initial conditions that may be specified on the boundary, $\partial\Omega$, or elsewhere. It should not be assumed, however, that reconstruction of the surface height function, $z = f(x, y)$, always is the goal in shape from shading. For example, orientation-based representations of surface shape can be used for object recognition and localization tasks [4, 5, 6, 9]. These representations use surface orientation directly, without computing the explicit representation of the object surface, $z = f(x, y)$.

Since Horn's original work, a substantial, but scattered literature on shape from shading has developed. Two essential references are Horn's text [26] and a collection of papers edited by Horn and Brooks [27]. With a single image, shape from shading problems typically are solved by exploiting *a priori* constraints on the reflectance map, $R(p, q)$, *a priori* constraints on surface curvature, or global smoothness constraints. Photometric stereo, on the other hand, makes use of additional images.

2.2 Photometric Stereo

Photometric stereo uses multiple images obtained under the identical geometry but under different conditions of illumination. Three image irradiance equations

$$\begin{aligned} E_1(x,y) &= R_1(p,q) \\ E_2(x,y) &= R_2(p,q) \\ E_3(x,y) &= R_3(p,q) \end{aligned} \tag{2}$$

in general overdetermine the solution at each point, (x,y), because three intensity measurements, $E_1(x,y)$, $E_2(x,y)$, and $E_3(x,y)$, are used to estimate two unknowns, p and q.

Conceptually, the implementation of photometric stereo is straightforward. Using a calibration object of known shape, one can build a lookup table mapping triples of measured brightness values, $[E_1, E_2, E_3]$, to the corresponding gradient, (p,q). Suppose each image is accurate to $2^8 = 256$ gray values. Then a full table would have $2^8 \times 2^8 \times 2^8 = 2^{24}$ entries. Despite advances in commercial hardware, a lookup table of this size still is prohibitive in terms of memory and real-time throughput capacity. The implementation described in Section 3 uses 2^6 gray values from each image as input to a lookup table with 2^{18} entries to achieve near real-time throughput at 15Hz.

2.2.1 Albedo Variation

A reflectance map determines measured intensity as a function of the surface gradient for a particular surface material, scene illumination and viewing geometry. If the material's bidirectional reflectance factor (i.e., albedo) also varies spatially, independent of the gradient, one would obtain

$$\begin{aligned} E_1(x,y) &= \rho(x,y)\, R_1(p,q) \\ E_2(x,y) &= \rho(x,y)\, R_2(p,q) \\ E_3(x,y) &= \rho(x,y)\, R_3(p,q) \end{aligned} \tag{3}$$

where $\rho(x,y)$ is the albedo, a function of (x,y). Thus, Equations (2) are a special case of Equations (3) in which the albedo is constant (and normalized to one). Equations (3) are three equations in the three unknowns, ρ, p and q. The equations generally are non linear so that a unique solution can not be guaranteed. For the Lambertian case, Equations (3) become linear when unit surface normals are used instead of the gradient to represent surface orientation, as shown in [2]. In this case, every triple of measured brightness values, $[E_1, E_2, E_3]$, determines a unique albedo, ρ, and gradient, (p,q).

It is useful to compare the formulation of photometric stereo given in Equations (2) with that used in Nayar *et. al.* [24]. Both use three light sources. Equations (2) are not restricted to the Lambertian case. Constant albedo is assumed and, as a consequence, the problem is overdetermined locally. Nayar's work is restricted to the Lambertian case. Albedo is allowed to vary since it is determined locally, in addition to the gradient. But, as Nayar *et. al.* point out, this determination is erroneous in the presence of interreflection. Errors can not be detected locally. Instead, the "pseudo shape" is defined to be the (possibly erroneous) shape and albedo determined by pointwise solution of the linearized version of Equations (3). They further show that this pseudo shape is unique for a given actual shape, independent of the illumination and viewpoint. Finally, they demonstrate an iterative algorithm to reconstruct a possible actual shape and albedo from the measured pseudo shape. This iterative algorithm is non local, requiring explicit reconstruction of the surface height function, $z = f(x, y)$, at each iteration step.

The comparison now is clear. Both local solutions are subject to error in the presence of interreflection and cast shadows. When the problem is not overdetermined, as with Nayar *et. al.*, there is little one can do locally to detect errors. Their approach necessarily requires global analysis. On the other hand, when the problem is overdetermined, as is the case with Equations (2), it becomes possible also to locally detect inconsistencies.

A key benefit of using multiple light sources is the ability to overdetermine the problem locally. If one needs to account for spatially varying albedo, as in Equations (3), it is possible to use a fourth light source, as suggested early on [28]. The idea is to define three ratio images $\hat{E}_i = E_i/E_4$, with associated reflectance maps $\hat{R}_i = R_i/R_4$, using the fourth image, E_4, as reference. Using ratios, the four light source case becomes equivalent to the constant albedo three light source case, given by Equations (2), because the spatially varying albedo terms cancel when the ratios are formed. Once the gradient is determined locally, the albedo also can be determined. (In practice, it is preferable to define $\hat{E}_i = (E_i - E_4)/(E_i + E_4)$ so that $\hat{R}_i = (R_i - R_4)/(R_i + R_4)$ but the idea is the same).

In this paper, constant albedo is assumed so that three light source photometric stereo is characterized by Equations (2). When albedo varies, as in Equations (3), the problem can be reduced to the form of Equations (2) by using a fourth light source and ratioed images, as indicated. If the albedo also depends on imaging geometry, then the image irradiance equations become $E_i(x, y) = R_i(p, q, \rho)$, $i = 1, 2, 3, 4$. Ratioing no longer suffices. Nevertheless, measured intensities are constrained to lie on a 3D manifold in the 4D space of possibilities, demonstrating that the solution still is overdetermined locally.

2.3 2D Surfaces in the 3D Space of Measured Intensities

Equations (2) define the parametric equations, in parameters p and q, of a 2D surface in the 3D coordinate space whose axes are E_1, E_2 and E_3. Thus, with constant albedo and no interreflection nor cast shadows, triples of measured intensity values, $[E_1, E_2, E_3]$, are constrained to lie on a 2D surface in any three light source photometric stereo situation. This 2D surface exists independent of the particular parameterization. When parameterized in terms of the gradient, (p, q), the equations take on the form given by Equations (2).

2.3.1 Example: Lambertian Reflectance

When an ideal Lambertian material is illuminated by a single distant light source, image irradiance is proportional to $\cos(i)$, where i is the *incident angle* (i.e., the angle between the surface normal and a vector in the direction to the light source).

Figure 1 shows the scatterplot obtained for Lambertian reflectance corresponding to three different directions of equal strength distant point source illumination. The gradients corresponding to the light source directions for $E_1(x, y)$, $E_2(x, y)$ and $E_3(x, y)$ are, respectively, $(0.7, 0.3)$, $(-0.7, 0.3)$ and $(0, 0)$.

In Figure 1 and in all the scatterplots that follow, the 2D surface is shown as an empirical point plot of measured intensity triples, $[E_1, E_2, E_3]$. E_1, E_2 and E_3 define the axes of a right-handed Euclidean coordinate system. One can think of the E_1-axis as pointing east, the E_2-axis as pointing north and the E_3-axis as pointing up. Scatterplots are displayed as orthographic projections from a given viewing direction. The viewing direction is specified by an elevation and azimuth. Elevation is the angle above the ground (i.e., $E_1\,E_2$) plane and azimuth is measured clockwise from north (i.e., clockwise from the E_2-axis). Throughout, two particular viewing directions are used: (a) elevation=10.0 azimuth=225.0 and (b) elevation=0.0 and azimuth=0.0. (All angles are in degrees). View (a) corresponds to a low "altitude" view from the southwest and view (b) corresponds to a projection onto the $E_1\,E_3$ plane. (The E_2-axis points directly at the viewer).

The 2D surface depicted in Figure 1 is a six degree of freedom ellipsoid. The particular ellipsoid is determined by the relative strength and configuration of the three light sources. (Appendix A derives this result). The ellipsoid does not depend on the shape of the object in view nor on the relative orientation between object and viewer.

2.3.2 Example: Phong Reflectance

The reflectance of many materials is modeled as a combination of a diffuse component and a specular component. In recent years, considerable progress has been made to formulate models based on principles of optics [25]. One early model, well-known in both computer vision and graphics, is Phong shading. Phong shading is a purely phenomenological model that now is considered inadequate since, for example, it fails to satisfy Helmholtz's law of reciprocity [29]. A variant of Phong shading described in [30, Section XXXIX]) does satisfy reciprocity. Image irradiance is proportional to

$$\frac{\cos(i)\,[(1-\alpha)+\alpha\cos^n(s/2)]}{\cos(g/2)}$$

where i, as before, is the incident angle, g is the *phase angle* (i.e., the angle between the vector pointing to the light source and the vector pointing to the viewer), s is the *off-specular angle* (i.e., the angle between the vector pointing to the viewer and the vector that defines, relative to the light source direction and the surface normal, the direction of perfect specular reflection), α is a fraction, $0 \le \alpha \le 1$, that models how much of the incident light is reflected specularly and n is a number that models how compact the specular patch is about the direction of perfect specular reflection. Parameters α and n vary according to the properties of the material modeled. Phong shading is used here only for illustrative purposes.

Figure 2 shows the scatterplot obtained for Phong reflectance ($\alpha = 0.75$ and $n = 20$) in the same three light source configuration used for the Lambertian case, Figure 1. The 2D surface defined still is smooth but clearly it no longer is an ellipsoid. Similar results would be noted for other non-Lambertian reflectance models [25].

2.4 Surface Curvature

The principal curvatures, and measures derived from principal curvature, are viewpoint invariant and therefore play a potentially valuable role in shape representation for tasks including surface segmentation, object recognition, attitude determination and surface reconstruction. In differential geometry, there are a variety of representations from which principal curvatures can be determined. Many are derived from the explicit surface height representation, $z = f(x,y)$. Here, we develop representations for surface curvature based on the gradient, (p,q), the reflectance map, $R(p,q)$, and image intensity, $E(x,y)$. In particular, the goal is to determine what independent information about surface curvature can be extracted from the image irradiance equation.

There are three degrees of freedom to the curvature at a point on a smooth surface. Consequently, three parameters are required to specify curvature. One representation is in terms of the 2×2 matrix of second partial derivatives of the surface $z = f(x,y)$. For notational convenience, let

$$p_x = \frac{\partial^2 f(x,y)}{\partial x^2}, \;\; p_y = \frac{\partial^2 f(x,y)}{\partial x \partial y}, \;\; q_x = \frac{\partial^2 f(x,y)}{\partial y \partial x} \;\text{ and }\; q_y = \frac{\partial^2 f(x,y)}{\partial y^2}$$

Now, let **H** be the matrix,

$$\mathbf{H} \;=\; \begin{bmatrix} p_x & p_y \\ q_x & q_y \end{bmatrix}$$

H is called the *Hessian matrix* of $z = f(x, y)$. It may appear that four parameters are required to specify **H**. But, for smooth surfaces, **H** is symmetric. That is, $p_y = q_x$. Therefore, only three parameters are required after all. **H** is a viewer-centered representation of surface curvature because its definition depends on the explicit form of the surface function, $z = f(x, y)$, and on the fact that the viewer is looking in the positive Z direction.

From the Hessian, **H**, and the gradient, (p, q), one can determine a viewpoint invariant representation of surface curvature. Let **C** be the matrix,

$$\mathbf{C} \;=\; (1 + p^2 + q^2)^{-\frac{3}{2}} \begin{bmatrix} q^2 + 1 & -pq \\ -pq & p^2 + 1 \end{bmatrix} \mathbf{H} \tag{4}$$

Now, let k_1 and k_2 be the two eigenvalues of **C**, with associated eigenvectors ω_1 and ω_2. Then, k_1 and k_2 are the principal curvatures, with directions ω_1 and ω_2, at $z = f(x, y)$. The principal curvatures, k_1 and k_2, are viewpoint invariant surface properties since they do not depend on the viewer-centered XYZ coordinate system. Equation (4) determines principal curvatures from the Hessian matrix, **H**, and the gradient, (p, q). The terms in Equation (4) involving the gradient, (p, q), can be interpreted as the corrections required to account for the geometric foreshortening associated with viewing a surface element obliquely.

The directions ω_1 and ω_2 are viewpoint dependent. Although the directions of principal curvature are orthogonal in the object-centered coordinate system defined by the local surface normal and tangent plane, they are not, in general, orthogonal when projected onto the image plane. Thus, k_1, k_2, ω_1 and ω_2 together constitute four independent parameters that can be exploited. (Because they are viewpoint dependent, the directions ω_1 and ω_2 are not typically used in surface representations proposed for object recognition. Note, however, that Brady *et. al.* [31] argue that, in many cases, the lines of curvature form a natural parameterization of a surface).

Besl and Jain [32, 33] classify sections of a smooth surface into one of eight basic types based on the sign and zeros of Gaussian and mean curvature. The *Gaussian curvature*, K, also called the *total curvature*, is the product, $\mathrm{K} = k_1 k_2$, of the principal curvatures. The *mean curvature*, H, is the average, $\mathrm{H} = (k_1 + k_2)/2$, of the principal curvatures. It follows from elementary matrix theory that

$$\mathrm{K} \;=\; \det(\mathbf{C}) \quad \text{and} \quad \mathrm{H} \;=\; \frac{1}{2}\,\mathrm{trace}\,(\mathbf{C}) \tag{5}$$

The expression for K further simplifies to

$$\mathrm{K} \;=\; \frac{1}{(1 + p^2 + q^2)^2}\,\det(\mathbf{H}) \tag{6}$$

Thus, the sign of $\det(\mathbf{H})$ is the sign of the Gaussian curvature.

Other local curvature measures can be defined, as well. If k is a principal curvature then $r = 1/k$ is the associated radius of principal curvature. For a smooth surface, the first and second curvature functions are defined, respectively, as the sum of the principal radii of curvature and the product of the principal radii of curvature. For smooth surfaces, the second curvature function is equivalent to what's been called the Extended Gaussian Image (EGI) in computer vision [34]. These curvature functions possess desirable mathematical properties that can be exploited for object recognition and attitude determination [9, 35]. Koenderink also proposes two new curvature measures called curvedness and shape index [36].

Clearly, if one could locally determine the Hessian, **H**, then one could locally compute the curvature matrix, **C**, using the gradient, (p, q), obtained from photometric stereo and Equation (4). Given **C**, one could examine its eigenvalue/eigenvector structure to determine any local curvature representation involving the principal curvatures, k_1 and k_2, and their associated directions, ω_1 and ω_2, including Gaussian curvature, K, mean curvature, H, curvedness and shape index.

2.5 Determining the Hessian

It would seem that determining the Hessian, **H**, in photometric stereo requires nothing more than numerical differentiation of the gradient estimate, (p, q). While this may seem adequate, differentiating the gradient without prior global smoothing is unstable, especially if the gradient itself is inaccurate or if it has been quantized into too small a set of discrete values. Therefore, it is useful to determine what independent information about surface curvature can be extracted from the image irradiance equation.

By taking partial derivatives of the image irradiance Equation (1) with respect to x and y, two equations are obtained which can be written as the single matrix equation [10]

$$\begin{bmatrix} E_x \\ E_y \end{bmatrix} = \mathbf{H} \begin{bmatrix} R_p \\ R_q \end{bmatrix} \tag{7}$$

Subscripts x, y, p and q denote partial differentiation and the dependence of E on (x, y) and of R on (p, q) has been omitted for clarity. The vector $[E_x, E_y]$ is normal to the contour of constant brightness in the image at the given point (x, y). The vector $[R_p, R_q]$ is normal to the contour of constant brightness in the reflectance map at the given gradient (p, q). Equation (7) alone is not enough to determine the Hessian, **H**. But, with photometric stereo, one such equation is obtained for each image. In a two light source case, one obtains

$$\mathbf{H} = \begin{bmatrix} E_{1x} & E_{2x} \\ E_{1y} & E_{2y} \end{bmatrix} \begin{bmatrix} R_{1p} & R_{2p} \\ R_{1q} & R_{2q} \end{bmatrix}^{-1} \tag{8}$$

provided the required matrix inverse exists. In the three light source case, the problem once again is overdetermined. One can write

$$\mathbf{H} = \begin{bmatrix} E_{1x} & E_{2x} & E_{3x} \\ E_{1y} & E_{2y} & E_{3y} \end{bmatrix} \mathbf{R} \tag{9}$$

where

$$\mathbf{R} = \mathbf{M} \left(\mathbf{M}^T \mathbf{M}\right)^{-1}$$

(^{T} denotes matrix transpose) and

$$\mathbf{M} = \begin{bmatrix} R_{1p} & R_{1q} \\ R_{2p} & R_{2q} \\ R_{3p} & R_{3q} \end{bmatrix}$$

provided the required matrix inverse exists. Equation (9) is the standard least squares estimate of the solution to an overdetermined set of linear equations. It can be extended, in the obvious way, to situations in which more than three light sources are used.

The matrices **M** and **R** are matrix functions of the gradient, (p, q). They depend only on the three reflectance maps, $R_i(p, q)$, $i = 1, 2, 3$. The matrix function **R** can be determined at the time of gradient lookup table calibration. It too can be thought of as a (large) lookup table, indexed by the gradient, (p, q). The matrix $\mathbf{M}^T\mathbf{M}$, whose inverse is required, is independent of the three images, $E_i(x, y)$, $i = 1, 2, 3$, and hence independent of the particular surface in view. Thus, for a particular surface material, the principal factor that determines the existence and robustness of the computation is the nature and the distribution of the light sources. No useful local information is obtained when $[R_p, R_q]$ is zero. This occurs at local extrema of $R(p, q)$ and at gradients, (p, q), shadowed from the light source. There also may be gradients, (p, q), where two of the three $[R_p, R_q]$ vectors are nearly parallel. Local degeneracies in the two light source configuration can be eliminated (and the effects of shadows minimized) when three, rather than two, light source photometric stereo is used.

In Equation (9) the magnitude of $[R_p, R_q]$ plays the role of a "weight" that pulls the three source solution towards an image irradiance equation for which the magnitude of $[R_p, R_q]$ is large (and consequently away from an image irradiance equation for which the magnitude of $[R_p, R_q]$ is small). This has a desirable effect because locations in an image at which the magnitude of $[R_p, R_q]$ is small will contribute minimal information, and it is good that they are discounted. Because of this, points that are shadowed with respect to one of the light sources need not be considered as a special case. Indeed, when one of the $[R_p, R_q]$ vectors is zero, the three light source solution, given by Equation (9), reduces to the two light source solution, given by Equation (8).

The lookup table for gradient estimation, the reflectance maps, $R_i(p, q)$, $i = 1, 2, 3$, and the matrix $\mathbf{R}$ all are determined during calibration. Subsequently, on a pixel-by-pixel basis, the three local measurements of intensity, $[E_1, E_2, E_3]$, are used to estimate the gradient, (p, q). The six partial spatial derivatives of intensity, E_{ix}, E_{iy}, $i = 1, 2, 3$, together with the gradient, (p, q), are used to estimate the three parameters of the Hessian, p_x, q_y and $p_y = q_x$. Thus, a total of nine independent local measurements are used to estimate a total of five local parameters. The estimate of the Hessian, $\hat{\mathbf{H}}$, is not strictly independent of the estimate of the gradient, (p, q), since the gradient is required to determine the appropriate value of the matrix $\mathbf{R}$ for Equation (9). Nevertheless, the matrix $\mathbf{R}$ tends to be robust with respect to errors in the gradient, (p, q), since, except in regions of highlight or specularity, the error in $[R_p, R_q]$ tends to be small for a given error in (p, q).

Given that estimation of the Hessian is overdetermined, it also becomes possible locally to detect when curvature estimation is unreliable. In previous work [15], two approaches were described. First, recall that symmetry of the Hessian, $\mathbf{H}$, corresponds to the smoothness (i.e., integrability) of the underlying surface, $z = f(x, y)$. When Equation (9) is applied, it is unlikely that the resulting estimate of the Hessian, $\hat{\mathbf{H}}$, is exactly symmetric. Symmetry is forced by projecting $\hat{\mathbf{H}}$ onto the so-called symmetric part of $\hat{\mathbf{H}}$, given by

$$\frac{\hat{\mathbf{H}} + \hat{\mathbf{H}}^T}{2} \tag{10}$$

prior to estimating the curvature matrix, $\mathbf{C}$, with Equation (4). The assumption that the surface locally is integrable can be tested by comparing the norm of the symmetric part of $\hat{\mathbf{H}}$ to that of the anti-symmetric part given by

$$\frac{\hat{\mathbf{H}} - \hat{\mathbf{H}}^T}{2}$$

Second, one can determine how well the estimated Hessian, $\hat{\mathbf{H}}$, accounts for the measured intensity gradients, $[E_{ix}, E_{iy}]$, $i = 1, 2, 3$, based on the error matrix, $\mathbf{E} = [e_{ij}]$, defined by

$$\mathbf{E} = \begin{bmatrix} E_{1x} & E_{2x} & E_{3x} \\ E_{1y} & E_{2y} & E_{3y} \end{bmatrix} - \hat{\mathbf{H}} \begin{bmatrix} R_{1p} & R_{2p} & R_{3p} \\ R_{1q} & R_{2q} & R_{3q} \end{bmatrix}$$

3 Implementation and Experimental Results

3.1 Experimental Setting

A calibrated imaging facility (CIF) has been built to control both scene parameters and conditions of imaging. It is based on a 4' × 8' optical bench with mounting hardware for controlled positioning and motion of cameras, light sources and test objects. Specialized equipment includes: a Sony DXC-755 3 CCD 24-bit RGB camera with Fujicon 10–120mm (manual) zoom lens; three Newport MP-1000 Moire (white light) projectors with associated Nikon lenses and spectral filters; two Daedal rail tables (one 36" and the other 6") and one Daedal rotary table (6"); and associated controllers, motors, mounting hardware and power supplies. The facility is well integrated with the other vision and robotics equipment in the UBC Laboratory for Computational Intelligence, including a Datacube image processing system consisting of DigiColor and MaxVideo-200 subsystems.

Work on photometric stereo and related work on multiple light source optical flow [37] requires multiple images of a scene acquired simultaneously under different conditions of illumination. This is achieved by multiplexing the spectral dimension. With appropriate filtration, the three projectors become spectrally distinct lights sources, one red, one green and one blue. The three color separation filters used are the Newport FS-225 set. The filters are manufactured by Corion, Corp., Holliston, MA, and carry Corion part numbers CA500 (blue), CA550 (green) and CA600 (red). The projectors illuminate the work space from different directions. The Sony 3 CCD RGB camera is used to simultaneously acquire three separate B&W images, one corresponding to each condition of illumination.

Care has been taken to ensure that the equipment achieves its intended functionality. The light sources and associated lenses are rated to produce an illumination field uniform to within ±10% over half the spot diameter and uniform to within ±15% over the full spot diameter. The light sources also are DC powered to eliminate the effects of 60Hz AC line flicker. When experiments are in progress, the CIF is enclosed by floor to ceiling black curtains thus isolating it from other light sources in the laboratory.

The precise spectral response of each of the filters has been measured by the manufacturer. There is negligible overlap in the visible spectrum between the red light source and either the green light source or the blue light source. There is a small overlap between the green and the blue light sources for wavelengths in the 500–520nm range. Clearly, if either the camera's green channel or its blue channel is sensitive to this common region, there will be some overlap between the images acquired. Indeed, if the camera's spectral responses are quite broad, overlap is possible even if the light sources themselves do not overlap spectrally. Unfortunately, the precise spectral response of camera is not provided by manufacturer nor has it been measured. Instead, a simple test was performed to estimate the response of the RGB camera channels in the given experimental setting. Three RGB video frames were acquired for a test scene consisting of a simple white object. In frame 1, only the red light source was on. In frame 2 only the green light source was on and in frame 3 only the blue light source was on. The correlation coefficient between the illuminated channel and the other two channels was determined for each frame. The correlation coefficient is a measure of the linear relationship between the two channels. One useful interpretation is that the square of the correlation coefficient is the proportion of the variance accounted for by linear regression. Let $X \rightarrow Y$ denote the influence of light source X on camera channel Y. In four cases, $R \rightarrow G$, $R \rightarrow B$, $B \rightarrow R$ and $G \rightarrow B$, the variance accounted for was less than 1% indicating excellent spectral separation. In the remaining two cases, the variance accounted for was higher indicating some spectral overlap. The result was 3.5% for $G \rightarrow R$ and 6.5% for $B \rightarrow G$. The slight effect of this overlap is noted in the examples that follow.

Two objects are used in the experiments reported. One is a pottery sphere, used for calibration purposes, and the other is a pottery doll face. In this case, both objects are made of the same material with the same reflectance properties. Pottery, in bisque form, is a reasonably diffuse reflector although no particular assumption is made (or required) concerning the underlying surface reflectance function. Other objects made of other materials have been used in experiments too. For each material, a different calibration sphere is required. In some cases, paint was used to achieve the effect of having a calibration sphere and object made of the same material. Although many different objects have been tested and many experiments run, the examples used here, following calibration, all come from an eleven frame sequence during which the doll face was rotated exactly 3 degrees (about the vertical axis) between successive frames.

3.2 Calibration

Calibration measures reflectance data using an object of known shape. These measurements support the analysis of other objects provided the other objects are made of the same material and are illuminated and viewed under the same imaging conditions. Empirical calibration has the added benefit of automatically compensating for the transfer characteristics of the sensor. Ideally, the calibration object is convex, to eliminate interreflection, and has visible surface points spanning the full range of gradients, (p, q). A sphere is a good choice and is the calibration shape used here. For a sphere, it is straightforward to determine the gradient, (p, q), and the Hessian matrix, $\mathbf{H}$, at each visible surface point by geometric analysis of the object's boundary contour. Figure 3(a–c) shows the three images of the calibration sphere obtained from the three different light source directions. The sphere appears as an ellipse because camera calibration, and in particular aspect ratio correction, has not been applied. Nevertheless, the object's boundary contour is easily determined (and becomes part of camera geometric calibration). Let λ denote the relative scaling (i.e., the aspect ratio) of y compared to x. Then, the equation of the sphere centered at the origin with radius r is

$$x^2 + (\lambda\, y)^2 + z^2 = r^2$$

Again, the standard geometry of shape from shading is assumed. That is, the object is defined in a left-handed Euclidean coordinate system where the viewer is looking in the positive Z direction, image projection is orthographic, and the image XY axes coincide with the object XY axes. Then, the gradient and Hessian at point (x, y) are respectively

$$p \;=\; -\frac{x}{z} \quad \text{and} \quad q \;=\; -\frac{\lambda^2\, y}{z}$$

$$\mathbf{H} \;=\; -\frac{1}{z^3} \begin{bmatrix} r^2 - \lambda^2 y^2 & \lambda^2 xy \\ \lambda^2 xy & \lambda^2 (r^2 - x^2) \end{bmatrix}$$

Processing the calibration images involves three steps. First, the three images are summed. This is done to make sure that no part of the object's boundary is missed because it lies in shadow. Second, an intensity histogram of the sum image is computed and a threshold is selected to separate object from background. Simple thresholding is sufficient since, by design, the object is distinct from the black background (i.e., the histogram is clearly bimodal). Third, a simple least squares method is used to estimate the equation of the ellipse which best fits the object boundary. The equation of the ellipse establishes the relation between (x, y) and (p, q) for all points on the calibration object (and, as a side-effect, determines λ).

Estimation of the ellipse is robust because all boundary points contribute. Figure 3(d) shows the fitted ellipse overlayed on the sum image. (A small portion near the bottom of the ellipse does not figure in the calculation since it corresponds to a region of the sphere obscured by the fixture used to hold the object). Figure 3 represents a 256×256 subwindow of the full 512×480 video frame. A total of 566 boundary points contribute to estimation of the ellipse. As a measure of the goodness of fit, the perpendicular distance of each boundary point from the ellipse was calculated. The mean perpendicular distance was 0.429 pixels and the standard deviation was 0.367.

Figure 4 shows the scatterplot obtained for the calibration sphere. The intensity triples, $[E_1, E_2, E_3]$, lie on a single 2D surface. (For comparison purposes, see Figure 5, the scatterplot for frame 5 of the doll face sequence. The comparison is discussed in Section 3.6). If one chose to force a constant albedo Lambertian model onto this example, one could fit an ellipsoid to the data shown in Figure 4. This has been done, as an exercise, and, while the details are not reported here, it is fair to conclude that the result is inferior to the non-parametric approach (that makes no Lambertian assumption and requires no radiometric correction for the transfer characteristics of the sensor).

3.3 Lookup Tables for Real-Time Photometric Stereo

Lookup table construction consists of three parts. First, the initial mapping between triples of measured intensity values, $[E_1, E_2, E_3]$, and surface orientation is established. Second, table interpolation is used to ensure that the 2D surface defined in the 3D space of measured intensity triples is simply connected. Third, morphological dilation (i.e., expansion) of the table is used to generate surface orientation estimates for intensity triples, $[E_1, E_2, E_3]$, that do not fall directly on the 2D calibration surface. As part of lookup table expansion, a distance measure is recorded that determines how far each new point is from a direct table hit. This distance measure, in turn, is used to define the local confidence estimate.

For real-time implementation, the lookup table is of dimension $2^6 \times 2^6 \times 2^6 = 2^{18}$. During calibration, surface orientation is represented by a unit surface normal rather than by the gradient. Each pixel location on the calibration object is sampled. The intensity triple, $[E_1, E_2, E_3]$, is constructed by taking the high order 6 bits from each of the 8-bit values for $E_1(x, y)$, $E_2(x, y)$ and $E_3(x, y)$. The result defines an 18-bit lookup table index. The unit surface normal corresponding to $[E_1, E_2, E_3]$ is calculated using the equation of the fitted ellipse. The unit surface normal is arithmetically added to the table. Summing unit surface normals averages the triples, $[E_1, E_2, E_3]$, that occur more than once on the calibration object. (As a post-processing step, the summed surface normal vectors are renormalized to unit vectors). This completes part one of lookup table construction.

It also is likely that there are "gaps" in the lookup table. This happens, for example, when intensity varies rapidly enough that the distance between neighboring triples, $[E_1, E_2, E_3]$, is greater than one in either the E_1, E_2 or E_3 dimension. In part two of lookup table construction, these gaps are detected and intermediate table entries are interpolated by sub-pixel resampling of the calibration images. At the end of part two, the 2D calibration surface is simply connected and all table entries are deemed distance $d = 0$ (i.e., direct hit) entries.

In part three, the lookup table is iteratively expanded n times to extrapolate entries at distances $d = 1, 2, \ldots, n$ from the 2D calibration surface. Let $[i, j, k]$ be a table index at the d^{th} iteration that has no current entry (i.e., no surface normal assigned). The six neighboring points, $[i \pm 1, j \pm 1, k \pm 1]$ are examined. If exactly one of the six neighbors is a table entry then $[i, j, k]$ is added to the table as a new distance d entry with surface orientation equal to that of the neighbor. (If more than one of the neighbors are table entries then $[i, j, k]$ is added to the table as a new distance d entry with surface orientation a weighted average of the surface normals of those neighbors where the weights are inversely proportional to the distances assigned to those neighbors).

If iterative expansion were allowed to run to completion, then every table entry would record a unit surface normal and a distance, d, corresponding to the iteration at which the surface normal was assigned. In the experiments that follow, $n = 10$ iterations were performed. Intensity triples that have no table entry become points at which photometric stereo assigns no gradient. A bitmap file can be produced to mark those points at which no gradient, (p, q), was assigned.

Figure 6 is a conceptual diagram of how the near real-time implementation is achieved on the Datacube system. The 24-bit RGB camera output is converted to a $2^6 \times 2^6 \times 2^6 = 2^{18}$ table index by combining the high-order 6 bits of R, G and B. The lookup table supports two independent 8-bit output streams. In the mode of operation depicted in Figure 6, one 8-bit stream is an index to a colormap used to render the gradient, (p, q), and the other 8-bit stream is the gray value representing the distance, d. If things were indeed this simple, the implementation would be straightforward. Unfortunately, the Datacube MaxVideo-200 does not have a lookup table of length 2^{18}, as depicted. It does, however, have four lookup tables of length 2^{16}. In the actual implementation, the high-order 2 bits of the R image are used as a selector to determine which of the four lookup tables of length 2^{16} to use. The MaxVideo-200 operates internally at field rates (i.e., 60Hz). It is possible to split the incoming video stream, pass it through the four lookup tables and recombine it in a total of four field times leading to an overall throughput (on a 512 × 480 video frame) of 15Hz.

3.4 Determining the Reflectance Maps

Gradient estimation, via table lookup, does not determine the reflectance maps explicitly. But, curvature estimation needs their partial derivatives, with respect to p and q, to determine the matrix $\mathbf{R}$ of Equation (9). It is a simple matter to invert the calibration object gradient equations to determine the image point, (x, y), at which to obtain intensity measurements for any particular (p, q). In this way, the three reflectance maps, $R_i(p, q)$, $i = 1, 2, 3$, are interpolated from the calibration images. In the implementation, the reflectance maps are stored explicitly as arrays for a given domain of p and q and for a given grid spacing. The partial derivatives are computed from the interpolated reflectances maps, on demand. Figure 7 shows the three reflectance maps (with iso-brightness contours superimposed for illustration purposes). Tick marks on the (horizontal) p-axis and on the (vertical) q-axis are plotted one unit apart. Thus, the domain covered is approximately $-2.0 \leq p \leq 2.0$ and $-2.0 \leq q \leq 2.0$. Since the distance from the origin in gradient space, $\sqrt{p^2 + q^2}$, is the tangent of the slope angle, the domain covered includes all visible object points with slope relative to the image plane less than $\tan^{-1}(2.0) = 63.4$ degrees. (Again, a small region is missing that corresponds to the region of the sphere obscured by the fixture used to mount it for viewing).

3.5 Determining Surface Curvature

To determine surface curvature at a point, (x, y), we need to measure the six partial spatial derivatives, E_{ix}, E_{iy}, $i = 1, 2, 3$, and we need to estimate the gradient, (p, q). Reference data are the six partial derivatives, R_{ip}, R_{iq}, $i = 1, 2, 3$. The gradient, (p, q), is obtained via lookup table, as described in Section 3.3. The reflectance maps, $R_i(p, q)$, $i = 1, 2, 3$, are obtained as described in Section 3.4. In the current implementation, each image and reflectance map is smoothed with a 2D Gaussian and the required partial derivatives are estimated using simple local differencing. This computation has not yet been implemented in real-time.

At each object point where the gradient, (p, q), is estimated and where $R_i(p, q)$, $i = 1, 2, 3$ is defined, Equation (9) is used to estimate the Hessian matrix, $\mathbf{H}$. The resulting estimate, $\hat{\mathbf{H}}$, is made symmetric via Equation (10). The curvature matrix, $\mathbf{C}$, is determined using Equation (4). From the matrix $\mathbf{C}$, the principal curvatures, k_1 and k_2, their associated directions, ω_1 and ω_2, and other curvature measures are derived, as described in Section 2.4. Again, none of these curvature computations has yet been implemented in real-time.

3.6 Experimental Results

For experimental and demonstration purposes, a particular color encoding for the gradient has been adopted. Figure 8 shows the three input images for frame 5 of the doll face sequence.

The figure shows a 384×256 subwindow extracted from the full video frame. Light sources 1, 2 and 3 correspond, respectively, to the red, green and blue illuminants. Evidence that the blue light source some has influence on the green channel, but negligible on the red, is noted in that the neck shadow region in Figure 8(b) is not as dark as the corresponding shadow region in Figure 8(a). Figure 9 shows the corresponding color encoded gradient as produced in the near real-time (15Hz) implementation of photometric stereo. The inset (lower right) shows the color rosette used to encode the gradient. The white lines in the center row and center column of the rosette represent, respectively, the p and the q axes. Angular position about the origin is encoded as color and distance from the origin is encoded as brightness. The domain of (p, q) covered is $-1.5 \leq p \leq 1.5$ and $-1.5 \leq q \leq 1.5$ so that points with slope less than or equal to $\tan^{-1}(1.5) = 56.3$ degrees are encoded by distinct colors and brightnesses. The color encoding demonstrates qualitatively the local effectiveness of photometric stereo, as can be seen, for example, around the hollow eye sockets. At the circumference of each eye socket, it is evident that the local surface slope and aspect has been recovered.

For integration with other vision modules, it is useful to use the two lookup table output streams to carry 8-bits each of p and q. This is a trivial modification to what has been described. The necessary information is available from calibration and the change simply means that a different lookup table is loaded into the MaxVideo-200.

Figure 5, shows the scatterplot obtained for the three images of the doll face (frame 5) shown in Figure 8. Clearly, it can no longer be said that all intensity triples, $[E_1, E_2, E_3]$, lie on a single 2D surface. Even though the doll face is made of the same material and is illuminated in the same way, it is a more complex shape than the calibration sphere. It is non convex with regions of cast shadow and regions where interreflection is significant.

Figure 10 marks two regions for further scrutiny. The neck region has cast shadows in the light source 1 and 2 images (see Figure 8(a–b)). The nostril region has significant local interreflection. Figure 11 shows the scatterplot for the neck region. The outline of the calibration sphere scatterplot from Figure 4 is overlayed (in bold) for comparison purposes. It is clear that many of the points in the scatterplot are outliers with respect to the 2D surface defined by the calibration sphere. In particular, some points are darker in E_1 or E_2 than is consistent with their E_3 value. Similarly, Figure 12 shows the scatterplot for the nose region. Again, the outline of the calibration sphere scatterplot is overlayed (in bold) for comparison purposes. Many of the points in the scatterplot are outliers here too. In particular, many points are brighter than is consistent with the 2D calibration surface.

Figures 13, 14 and 15 show examples of gradient estimation from frames 0, 5 and 10 of the doll face sequence. In frame 5, the doll face is oriented directly towards the viewer. In frame 0 it is rotated $3 \times 5 = 15$ degrees to the left and in frame 10 it is rotated $3 \times 5 = 15$ degrees to the right. In these figures, the gradient is rendered in B&W. In each case, figure (a) encodes the slope angle (i.e., $\tan^{-1}(\sqrt{p^2 + q^2})$) as a gray value and figure (b) plots the aspect angle (i.e., $\tan^{-1}(q/p)$) as a short line segment. (To avoid clutter, the aspect angle is plotted for every fourth point in x and y). Slope and aspect are viewpoint dependent measures. Therefore the values for a given point on the doll face do not remain constant as the object rotates. Figure (c) encodes the distance measure, d, as a gray value. In particular, one can note that in Figure 14(c), the d value is large at many points in the neck and in the nostril region, confirming that these outliers have been detected.

Figures 16, 17 and 18 show examples of principal curvature estimation from frames 0, 5 and 10 of the doll face sequence. In each case, figure (a) encodes the first principal curvature, k_1, the curvature whose magnitude is maximum, and figure (b) encodes the second principal curvature, k_2, the curvature whose magnitude is minimum. Principal curvatures are viewpoint independent measures. Thus, the values for a given point on the doll face should remain constant as the object rotates. Figure (c) plots the corresponding principal directions, ω_1 (in bold) and ω_2. (To avoid clutter, the principal directions are plotted for every fifth point in x and y). The principal directions are viewpoint dependent.

4 Discussion and Conclusions

Multiple images acquired under the identical viewing geometry but different conditions of illumination are a principled way to obtain additional local constraint in shape from shading. Three light source photometric stereo is fast and robust. In the implementation described, surface gradient estimation is achieved on full frame video data at 15Hz using commercially available hardware. Surface curvature estimation also is demonstrated. Although not yet implemented in real-time, curvature estimation also is simple and direct, requiring no iteration steps. Overall, the computational requirements for photometric stereo are minimal compared to the iterative schemes typically required for shape from shading from a single image. The main practical limits on system performance are data storage, required by calibration, and data throughput, required to process multiple images, including spatial derivatives, simultaneously.

One practical benefit of real-time implementation is the ability to integrate photometric stereo and motion (based on related work on multiple light source optical flow [37]). A high-speed camera shutter setting ensures that all surfaces points are imaged at essentially the same instant in time. Real-time implementation of both photometric stereo and optical flow can then determine the 3D structure and the 3D motion of deforming objects. Another benefit relates to tasks where it may neither be possible nor appropriate to use alternatives, such as laser range sensors. For example, photometric stereo is being evaluated for a medical application involving the acquisition of 3D models of children's faces (used to plan subsequent medical procedures). Here, data acquisition must not harm the patient (so that the use of laser ranging is problematic). Since children typically do not stay stationary, data acquisition also must be rapid.

Photometric stereo achieves robustness in several ways. The key is to overdetermine the problem locally. Overdetermination provides noise resilience and protection against local degeneracies. To specify the local properties of a surface up to curvature requires six parameters since there is one degree of freedom for range, two for surface orientation and three for curvature. If only a single measurement, say range, is available locally, then the problem is locally underconstrained. The only solution then is to reconstruct a smooth surface globally by combining measurements obtained over extended regions. In three light source photometric stereo, each image provides three independent pieces of local information, one for intensity and two for the partial spatial derivatives of intensity. (To be truly independent, one would need an image sensor that measured partial derivatives directly). Thus, with three images one obtains nine local measurements to overdetermine the five unknowns associated with orientation and curvature. At the implementation level, gradient estimation is robust because 18 bits of RGB input are used to estimate 16 bits (8 bits each for p and q) of output.

Overdetermination also supports local detection of modeling errors and other inconsistencies. A (non parametric) empirical approach to reflectance modeling eliminates errors that arise when the experimental situation does not satisfy assumptions implicit in parametric models. It also eliminates the need to estimate the unknown parameters. For example, in the work described, one need never estimate the directions to the light sources nor their relative amplitudes. The empirical approach has the added benefit of automatically compensating for the transfer characteristics of the sensor. It also means that the system is robust to possible spectral overlap in the three color channels used. Indeed, complete spectral separation is not essential. At a higher level, robustness is achieved because an attempt is made to use of all the information available in an image, not just that obtained from a sparse set of features.

The claim that photometric stereo is accurate has not been dealt with quantitatively. A careful assessment of accuracy, including comparison with laser range sensors, is an essential next step. Proper error analysis, however, is non trivial. Issues involved include camera calibration (geometric and radiometric), method of integration (if comparison is made between depth values), range sensor calibration (if range data serves as ground truth) and method of differentiation (if comparison is made between gradients and differentiated range data).

Photometric stereo appears to be a competitive technique for a variety of tasks. One class of task is 3D model acquisition as, for example, required for computer graphics, CAD/CAM analysis and rapid prototyping. For this class of task, the accuracy of the reconstruction of the surface height function, $z = f(x, y)$, is central. But, surface reconstruction itself begs important questions. Standard schemes combine a data fit term with a global smoothness term. Smoothers typically used are viewpoint dependent. (Stevenson and Delp [38] is a notable exception). Reconstruction also requires specification of initial boundary conditions. In practice, the results of reconstruction tend to be dominated by the choice of smoother and by errors in the initial conditions. Given this, it is not clear what is the right approach to surface reconstruction when dense, accurate local orientation and curvature data are available.

Another class of task includes 3D object recognition, localization and inspection, as required, for example, in industrial automation. Photometric stereo has been used for object recognition and object localization in ways that do not reconstruct surface height, $z = f(x, y)$. In particular, Li [9] developed a system to determine the 3D attitude of known objects based on dense orientation and curvature data determined by photometric stereo. Her test objects were precision machined so that accuracy of attitude determination could be assessed. In the end, surface reconstruction may not be the sine qua non of shape from shading methods.

As shapes treated by machine vision and robotics systems become more complex, segmentation based on surface orientation and curvature becomes more important. Segmentation has always been a “chicken-and-egg” problem in computer vision. Three (or more) light source photometric stereo allows local surface orientation and curvature to be reliably estimated prior to segmentation. The redundancy in three light source photometric makes it possible also to detect local inconsistencies that arise, for example, due to cast shadows and interreflection. Detection is facilitated by expliciting including a local confidence estimate in the lookup table used for gradient estimation. The effective interaction between local estimation of surface properties, including local error detection, and global surface reconstruction remains to be explored. The hope is that the present work will allow future segmentation and integration schemes to be more robust.

Acknowledgement

The work described in this paper benefited from discussions with J. Arnspang, R.A. Barman, M.S. Drew, B.V. Funt, Y. Iwahori, Y. King, S. Kingdon, Y. Li, J.J. Little, D.G. Lowe, A.K. Mackworth, S.K. Nayar, M. Overton, J.M. Varah and L.B. Wolff. The original proof that the three light source Lambertian case defines an ellipsoid was joint with Y. Iwahori and R.A. Barman, as described in [39]. Subsequently, B.V. Funt pointed out that the result generalizes owing to the equivalence between any distant illumination and distant point source illumination for the Lambertian case. Y. Li and S. Kingdon programmed the real-time implementation of gradient estimation on the Datacube hardware. Major support for the research described was provided by the Institute for Robotics and Intelligent Systems (IRIS), one of the Canadian Network of Centres of Excellence; by the Natural Science and Engineering Research Council of Canada (NSERC); and by the Canadian Institute for Advanced Research (CIAR).

References

[1] R. J. Woodham, "Reflectance map techniques for analyzing surface defects in metal castings," AI-TR-457, MIT AI Laboratory, Cambridge, MA, 1978.

[2] R. J. Woodham, "Photometric method for determining surface orientation from multiple images," *Optical Engineering*, vol. 19, pp. 139–144, 1980. Reprinted in [27].

[3] W. M. Silver, "Determining shape and reflectance using multiple images," SM thesis, MIT Dept. Electrical Engineering and Computer Science, Cambridge, MA, 1980.

[4] K. Ikeuchi, "Recognition of 3-D objects using the extended Gaussian image," in *Proc. 7th Int. Joint Conf. on Artificial Intelligence*, pp. 595–600, 1981.

[5] P. Brou, "Using the Gaussian image to find the orientation of objects," *Int. J. Robotics Research*, vol. 3, no. 4, pp. 89–125, 1984.

[6] B. K. P. Horn and K. Ikeuchi, "The mechanical manipulation of randomly oriented parts," *Scientific American*, vol. 251, pp. 100–111, August 1984.

[7] K. Ikeuchi, B. K. P. Horn, S. Nagata, T. Callahan, and O. Feingold, "Picking up an object from a pile of objects," in *Robotics Research: The First International Symposium* (M. Brady and R. Paul, eds.), pp. 139–162, Cambridge, MA: MIT Press, 1984.

[8] K. Ikeuchi, H. K. Nishihara, B. K. P. Horn, P. Sobalvarro, and S. Nagata, "Determining grasp configurations using photometric stereo and the prism binocular stereo system," *Int. J. Robotics Research*, vol. 5, no. 1, pp. 46–65, 1986.

[9] Y. Li, "Orientation-based representations of shape and attitude determination," TR-93–12, UBC Dept. of Computer Science, Vancouver, BC, 1993.

[10] R. J. Woodham, "Analysing images of curved surfaces," *Artificial Intelligence*, vol. 17, pp. 117–140, 1981.

[11] M. A. Penna and S. S. Chen, "Shape-from-shading using multiple light sources," *Int. J. Intelligent Systems*, vol. 1, pp. 263–291, 1986.

[12] L. B. Wolff, "Surface curvature and contour from photometric stereo," in *Proc. DARPA Image Understanding Workshop, 1987*, pp. 821–824, 1987.

[13] L. B. Wolff, "Accurate measurement of second order variations of a smooth object surface using reflectance maps," in *Proc. SPIE Vol. 1003 Sensory Fusion: Spatial Reasoning and Scene Interpretation (1988)*, pp. 59–62, 1988.

[14] R. J. Woodham, "Determining surface curvature with photometric stereo," in *Proc. IEEE Conf. Robotics and Automation, 1989*, pp. 36–42, 1989.

[15] R. J. Woodham, "Surface curvature from photometric stereo," in *Physics-Based Vision: Principles and Practice (Vol III: Shape Recovery)* (L. Wolff, S. Shafer, and G. Healey, eds.), pp. 121–155, Boston, MA: Jones and Bartlett Publishers, Inc., 1992.

[16] K. Ikeuchi, "Determining surface orientation of specular surfaces by using the photometric stereo method," *IEEE Trans. Pattern Analysis and Machine Intelligence*, vol. 3, pp. 661–669, 1981.

[17] E. N. Coleman Jr. and R. Jain, "Obtaining 3-dimensional shape of textured and specular surfaces using four-source photometry," *Computer Graphics and Image Processing*, vol. 18, pp. 309–328, 1982.

[18] S. K. Nayar, K. Ikeuchi, and T. Kanade, "Determining shape and reflectance of hybrid surfaces by photometric sampling," *IEEE Transactions on Robotics and Automation*, vol. 6, no. 4, pp. 418–431, 1990.

[19] H. D. Tagare and R. J. P. de Figueredo, "A theory of photometric stereo for a class of diffuse non-Lambertian surfaces," *IEEE Trans. Pattern Analysis and Machine Intelligence*, vol. 13, no. 2, pp. 133–152, 1991.

[20] A. L. Gilchrist, "The perception of surface blacks and whites," *Scientific American*, vol. 240, pp. 112–124, 1979.

[21] B. K. P. Horn, "Understanding image intensities," *Artificial Intelligence*, vol. 8, pp. 201–231, April 1977.

[22] J. J. Koenderink and A. J. van Doorn, "Geometrical modes as a general method to treat diffuse interreflections in radiometry," *Journal of the Optical Society of America*, vol. 73, no. 6, pp. 843–850, 1983.

[23] D. Forsyth and A. Zisserman, "Reflections on shading," *IEEE Trans. Pattern Analysis and Machine Intelligence*, vol. 13, no. 7, pp. 671–679, 1991.

[24] S. K. Nayar, K. Ikeuchi, and T. Kanade, "Shape from interreflections," *Int. J. Computer Vision*, vol. 6, no. 3, pp. 173–195, 1991.

[25] L. Wolff, S. Shafer, and G. Healey, eds., *Physics-Based Vision: Principles and Practice (Vol I: Radiometry).* Boston, MA: Jones and Bartlett Publishers, Inc., 1992.

[26] B. K. P. Horn, *Robot Vision.* Cambridge, MA: MIT Press, 1986.

[27] B. K. P. Horn and M. J. Brooks, eds., *Shape from Shading.* Cambridge, MA: MIT Press, 1989.

[28] B. K. P. Horn, R. J. Woodham, and W. M. Silver, "Determining shape and reflectance using multiple images," AI-Memo-490, MIT AI Laboratory, Cambridge, MA, 1978.

[29] M. Minnaert, "The reciprocity principle in lunar photometry," *Astrophys. J.*, vol. 93, pp. 403–410, 1941.

[30] B. K. P. Horn, "Hill-shading and the reflectance map," *Proceedings of the IEEE*, vol. 69, pp. 14–47, 1981.

[31] M. Brady, J. Ponce, A. Yuille, and H. Asada, "Describing surfaces," *Computer Vision Graphics and Image Processing*, vol. 32, pp. 1–28, 1985.

[32] P. J. Besl and R. C. Jain, "Three-dimensional object recognition," *ACM Computing Surveys*, vol. 17, pp. 75–145, 1985.

[33] P. J. Besl and R. C. Jain, "Invariant surface characteristics for 3D object recognition in range images," *Computer Vision Graphics and Image Processing*, vol. 33, pp. 33–80, 1986.

[34] B. K. P. Horn, "Extended Gaussian images," *Proceedings of the IEEE*, vol. 72, pp. 1671–1686, 1984.

[35] Y. Li and R. J. Woodham, "The support function, curvature functions and 3-D attitude determination," in *Proc. IEEE Conf. Computer Vision and Pattern Recognition, 1993*, pp. 676–677, 1993.

[36] J. J. Koenderink, *Solid Shape.* Cambridge, MA: MIT Press, 1990.

[37] R. J. Woodham, "Multiple light source optical flow," in *Proc. 3rd International Conference on Computer Vision*, (Osaka, Japan), pp. 42–46, 1990.

[38] R. L. Stevenson and E. J. Delp, "Viewpoint invariant recovery of visual surfaces from sparse data," *IEEE Trans. Pattern Analysis and Machine Intelligence*, vol. 14, no. 9, pp. 897–909, 1992.

[39] R. J. Woodham, Y. Iwahori, and R. A. Barman, "Photometric stereo: Lambertian reflectance and light sources with unknown direction and strength," TR-91–18, UBC Dept. of Computer Science, Vancouver, BC, 1991.

[40] M. S. Drew, “Shape and specularity from color,” CSS/LCCR TR-93–01, Simon Fraser University, Burnaby, BC, 1993.

A Appendix: Lambertian Case (Constant Albedo)

This appendix reconsiders the case of three light source photometric stereo under the assumption of Lambertian reflectance and constant albedo. It is shown that, in the absence of interreflection and cast shadows, triples of measured intensity values determine a six degree of freedom ellipsoid. The ellipsoid characterizes the strengths and relative positions of the light sources.

The equation characterizing image irradiance for Lambertian reflectance, distant point source illumination, orthographic projection and transmittance through an intervening scatterless medium is,

$$E(x,y) \;=\; \frac{E_0}{\pi}\,\rho(x,y)\,cos(\theta_i) \tag{11}$$

where $E(x,y)$ is the measured irradiance at image point (x,y), $\rho(x,y)$ is the associated bidirectional reflectance factor (i.e., albedo), E_0 is the irradiance of the light source, and θ_i is the incident angle.

The original paper on photometric stereo [2] included a formulation to recover both surface gradient, (p,q), and surface reflectance, $\rho(x,y)$, under the assumptions of orthographic projection, three distant point sources of illumination and Lambertian reflectance. This is the basis for pseudo-shape recovery, as defined in [24]. To apply this result, however, it is necessary that the three light sources be in a known configuration and be of known strength.

Here, it is assumed that the directions to and the relative strengths of the light sources are not known. Estimation of these parameters becomes part of the problem formulation. Instead, it is assumed that $\rho(x,y)$ is constant at all object points of interest so that the dependence of ρ on (x,y) can be ignored. It follows, without loss of generality, that the scale factor in Equation (11) can be taken equal to 1 so that the image irradiance equation becomes the more familiar

$$E(x,y) \;=\; cos(\theta_i)$$

But, we want the relative strengths of the light sources to be distinct. Therefore, we write

$$E(x,y) \;=\; E\,cos(\theta_i) \tag{12}$$

where scalar parameter E characterizes the relative strength of the light source.

Directions can be represented by unit vectors so that the cosine of the angle between any two directions is the dot product of the corresponding two unit vectors. This allows the Lambertian case to be formulated as a linear problem. For three light source photometric stereo, let $\mathbf{a}_i \;=\; [a_{i1}, a_{i2}, a_{i3}]$, $i \;=\; 1,2,3$, be the 1×3 (row) vectors that point in the direction of light source i with magnitude equal to the relative strength, E_i, of light source i. Let $\mathbf{A}$ be the 3×3 matrix

$$\mathbf{A} \;=\; \begin{bmatrix} a_{11} & a_{12} & a_{13} \\ a_{21} & a_{22} & a_{23} \\ a_{31} & a_{32} & a_{33} \end{bmatrix}$$

Assume that the three light source directions, given by $\mathbf{a}_i$, $i \;=\; 1,2,3$, are not coplanar so that the matrix $\mathbf{A}$ is nonsingular.

Let $\mathbf{x} \;=\; [x_1, x_2, x_3]^T$ be the unit (column) surface normal vector at some object point of interest. Let $\mathbf{y} \;=\; [y_1, y_2, y_3]^T$ be the associated triple of intensity values given by Equation (12), applied once for each light source direction. Then, we obtain

$$\mathbf{y} \;=\; \mathbf{A}\,\mathbf{x} \tag{13}$$

Equation (13) establishes a linear relation between surface shape, given by the unit surface normal vector, $\mathbf{x}$, and measured intensity values, $\mathbf{y}$.

Of course, if we knew $\mathbf{A}$ then we could determine $\mathbf{x}$ as

$$\mathbf{x} = \mathbf{B}\,\mathbf{y} \tag{14}$$

where $\mathbf{B} = \mathbf{A}^{-1}$. Here, however, we do not assume that $\mathbf{A}$ is known. Fortunately, there is more that we can say simply based on the observation that Equation (13) is linear.

Consider each unit vector, $\mathbf{x}$, to be positioned at the origin. We can then associate all vectors, $\mathbf{x}$, with points on the unit sphere centered at the origin. In this way, we can think of Equation (13) as specifying a linear transformation of the sphere $\| \mathbf{x} \|_2 = (\mathbf{x}^T\mathbf{x})^{\frac{1}{2}} = 1$. It is reasonable to ask what is the corresponding shape defined by the vectors $\mathbf{y} = \mathbf{A}\,\mathbf{x}$.

Substitution, using Equation (14), shows that $\mathbf{x}^T\mathbf{x} = 1$ implies

$$(\mathbf{B}\,\mathbf{y})^T\,\mathbf{B}\,\mathbf{y} = \mathbf{y}^T\,\mathbf{B}^T\mathbf{B}\,\mathbf{y} = \mathbf{y}^T\,\mathbf{C}\,\mathbf{y} = 1$$

where $\mathbf{C} = \mathbf{B}^T\mathbf{B}$ is the 3×3 symmetric, positive definite matrix

$$\mathbf{C} = \begin{bmatrix} c_{11} & c_{12} & c_{13} \\ c_{21} & c_{22} & c_{23} \\ c_{31} & c_{32} & c_{33} \end{bmatrix} = \begin{bmatrix} \mathbf{b}_1{}^T\mathbf{b}_1 & \mathbf{b}_1{}^T\mathbf{b}_2 & \mathbf{b}_1{}^T\mathbf{b}_3 \\ \mathbf{b}_2{}^T\mathbf{b}_1 & \mathbf{b}_2{}^T\mathbf{b}_2 & \mathbf{b}_2{}^T\mathbf{b}_3 \\ \mathbf{b}_3{}^T\mathbf{b}_1 & \mathbf{b}_3{}^T\mathbf{b}_2 & \mathbf{b}_3{}^T\mathbf{b}_3 \end{bmatrix}$$

and where the $\mathbf{b}_i = [b_{1i}, b_{2i}, b_{3i}]^T$, $i = 1, 2, 3$, are the three 3×1 column vectors of $\mathbf{B}$.

Suppose we now measure intensity triples, $\mathbf{y}$, from points on an object of unknown shape. Then, these intensity triples are constrained to lie on the quadric surface $\mathbf{y}^T\,\mathbf{C}\,\mathbf{y} = 1$. That is, the intensity triples, $\mathbf{y}$, satisfy the equation

$$c_{11}\,y_1{}^2 + c_{22}\,y_2{}^2 + c_{33}\,y_3{}^2 + 2\,c_{12}\,y_1\,y_2 + 2\,c_{13}\,y_1\,y_3 + 2\,c_{23}\,y_2\,y_3 - 1 = 0 \tag{15}$$

This equation has six unknown coefficients. This follows, of course, from the fact that the matrix $\mathbf{C}$, being symmetric, has only six degrees of freedom. Equation (15) necessarily defines an ellipsoid because the matrix $\mathbf{C}$ is positive definite. In particular, $c_{ii} > 0$, $i = 1, 2, 3$.

In [39], a simple least squares method is used to estimate the six unknown coefficients of matrix $\mathbf{C}$ from scatterplots of measured intensity triples, even when the matrix $\mathbf{A}$ is unknown and even when the object shape also is unknown. The constraint that $\mathbf{C}$, in turn, imposes on $\mathbf{A}$ is easiest to interpret when expressed in terms of $\mathbf{C}^{-1}$. Let $\mathbf{D} = \mathbf{C}^{-1}$ so that

$$\mathbf{D} = \mathbf{C}^{-1} = (\mathbf{B}^T\mathbf{B})^{-1} = \mathbf{B}^{-1}(\mathbf{B}^T)^{-1} = \mathbf{B}^{-1}(\mathbf{B}^{-1})^T = \mathbf{A}\mathbf{A}^T$$

Therefore,

$$\mathbf{D} = \begin{bmatrix} d_{11} & d_{12} & d_{13} \\ d_{21} & d_{22} & d_{23} \\ d_{31} & d_{32} & d_{33} \end{bmatrix} = \begin{bmatrix} \mathbf{a}_1\mathbf{a}_1{}^T & \mathbf{a}_1\mathbf{a}_2{}^T & \mathbf{a}_1\mathbf{a}_3{}^T \\ \mathbf{a}_2\mathbf{a}_1{}^T & \mathbf{a}_2\mathbf{a}_2{}^T & \mathbf{a}_2\mathbf{a}_3{}^T \\ \mathbf{a}_3\mathbf{a}_1{}^T & \mathbf{a}_3\mathbf{a}_2{}^T & \mathbf{a}_3\mathbf{a}_3{}^T \end{bmatrix}$$

The matrix $\mathbf{D}$, like the matrix $\mathbf{C}$, is a 3×3 symmetric, positive definite matrix. From $\mathbf{D}$, one can determine the relative strengths of the light sources i, $i = 1, 2, 3$, and the angle between the vectors to light sources i and j, $i \neq j$, $i = 1, 2, 3$, $j = 1, 2, 3$. Specifically, the relative strength of light source i, E_i, is given by

$$E_i = (\mathbf{a}_i\mathbf{a}_i{}^T)^{\frac{1}{2}} = \sqrt{d_{ii}} \tag{16}$$

and the cosine of the angle, α_{ij}, $i \neq j$, between $\mathbf{a}_i$ and $\mathbf{a}_j$ is given by

$$cos(\alpha_{ij}) \;=\; \frac{\mathbf{a}_i {\mathbf{a}_j}^T}{\sqrt{\mathbf{a}_i {\mathbf{a}_i}^T}\,\sqrt{\mathbf{a}_j {\mathbf{a}_j}^T}} \;=\; \frac{d_{ij}}{\sqrt{d_{ii}}\,\sqrt{d_{jj}}} \tag{17}$$

Equations (16) and (17) together represent six constraints on the matrix $\mathbf{A}$. These six constraints can be interpreted geometrically. Let the vectors $\mathbf{a}_i$, $i \;=\; 1, 2, 3$, share a common origin. The vectors, $\mathbf{a}_i$, form a triad whose shape, specified by the lengths of the vectors and the angles between them, is known. Any rotation of this triad will not change the shape of the triad and therefore will not violate any of the six constraints. A 3D rotation has three degrees of freedom. To absolutely fix the triad in a given 3D coordinate system, three additional constraints would be required.

A simple mathematical argument demonstrates that the ellipsoid $\mathbf{y}^T\,\mathbf{C}\,\mathbf{y} \;=\; 1$ is, indeed, invariant under a rotation of the coordinate system used to represent $\mathbf{x}$. Let $\mathbf{R}$ be an arbitrary 3×3 rotation matrix. Consider rotating the unit surface normals by $\mathbf{R}$. That is, let $\hat{\mathbf{x}} \;=\; \mathbf{R}\,\mathbf{x}$ Clearly, the constraint $\hat{\mathbf{x}}^T\hat{\mathbf{x}} \;=\; 1$ is preserved since

$$\hat{\mathbf{x}}^T\hat{\mathbf{x}} \;=\; (\mathbf{R}\,\mathbf{x})^T\mathbf{R}\,\mathbf{x} \;=\; \mathbf{x}^T(\mathbf{R}^T\mathbf{R})\mathbf{x} \;=\; \mathbf{x}^T\mathbf{x} \;=\; 1$$

Therefore, the corresponding constraint $\mathbf{y}^T\,\mathbf{C}\,\mathbf{y} \;=\; 1$ also is preserved. It should not be surprising that the ellipsoid $\mathbf{y}^T\,\mathbf{C}\,\mathbf{y} \;=\; 1$ is invariant under a rotation of the object being viewed since the brightness of a Lambertian reflector is independent of viewpoint.

Finally, there is a generalization to the derivation given here that merits attention. The matrix $\mathbf{A}$ characterizes the directions to and the relative strengths of three distant point light sources. It is natural, therefore, to assume that the derivation is valid only when there literally are three distant point light sources. In fact, the result holds more generally as a consequence of another property of Lambertian reflectance. For any Lambertian surface and any spatial distribution of distant illumination, there exists a single distant point source that produces the same reflectance map for that region of the gradient space not self-shadowed with respect to any part of the illuminant. Silver [3, pp 104–105] provides a formal derivation of this property. The derivation is not repeated here.

Lambertian shading from surface points not shadowed with respect to any part of a spatially distributed distant illuminant is equivalent to that obtained from a single distant point source illuminant. Silver's derivation is constructive. Given any spatially distributed distant illuminant, one can determine the equivalent point source direction and strength. Thus, for Lambertian reflectance, triples of measured intensity values determine a six degree of freedom ellipsoid, even if one or more of the three images arises from a spatially distributed illuminant. The ellipsoid then characterizes the strengths and relative positions of the three equivalent distant point light sources. Recently, Drew [40] has used this idea to demonstrate that it is possible to recover surface shape from color images of Lambertian surfaces given that a spatially distributed distant illuminant also varies spectrally. Drew also argues that the underlying ellipsoid arising from Lambertian reflectance can be recovered in the presence of specularities provided that specular points can reliably be detected as outliers. But, it is not clear, given the example of Phong reflectance shown in Figure 2, that specularities always can be effectively treated as outliers to an underlying ellipsoid shape.

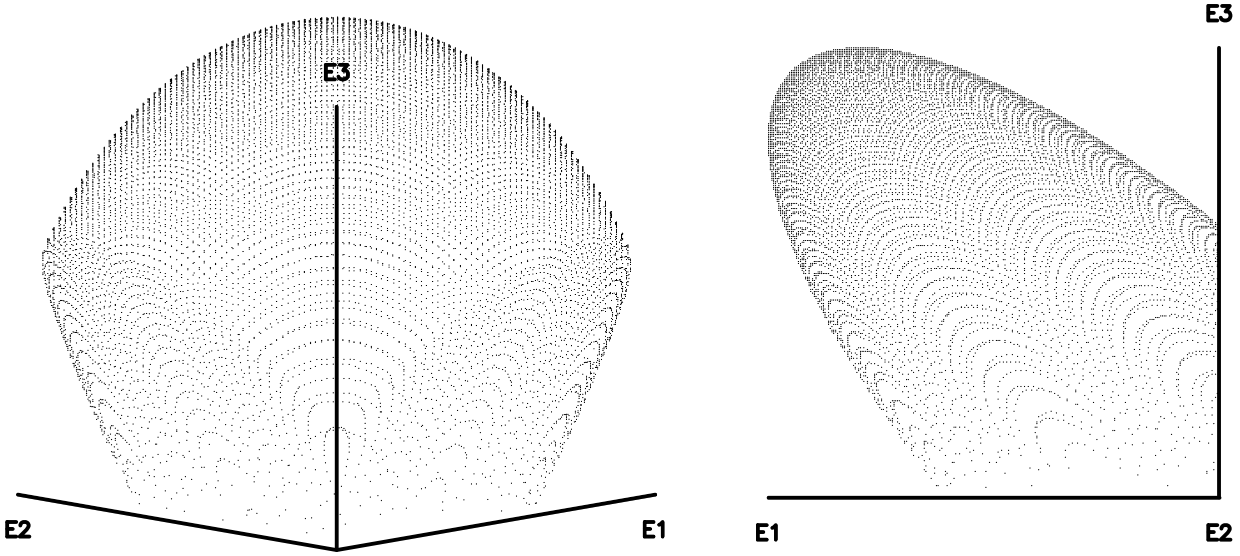

(a) elevation 10.0 azimuth 225.0

(b) elevation 0.0 azimuth 0.0

Figure 1: Lambertian reflectance: scatterplot of measured intensity triples.

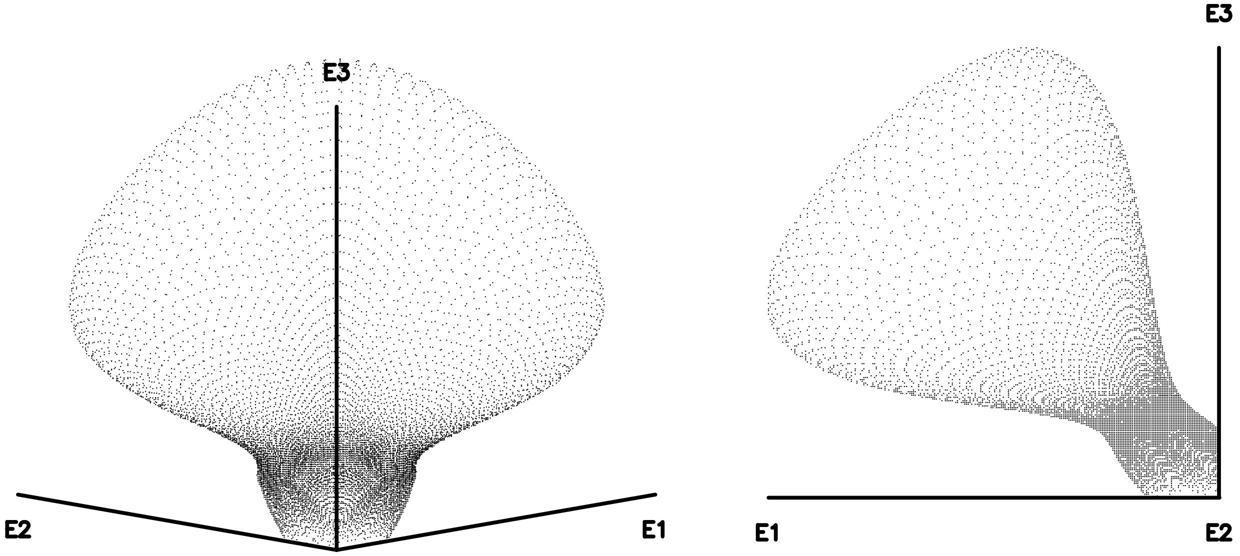

(a) elevation 10.0 azimuth 225.0

(b) elevation 0.0 azimuth 0.0

Figure 2: Phong reflectance: scatterplot of measured intensity triples.

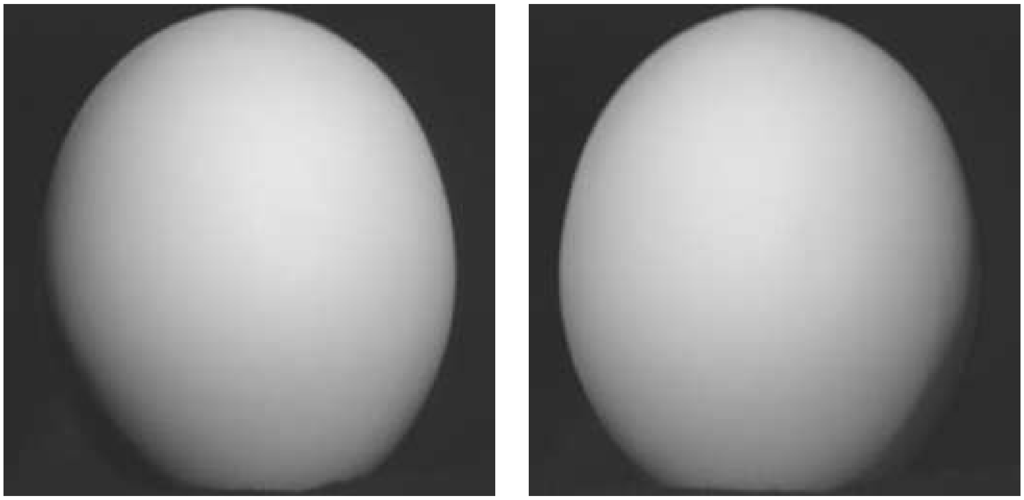

(a) Light source 1

(b) Light source 2

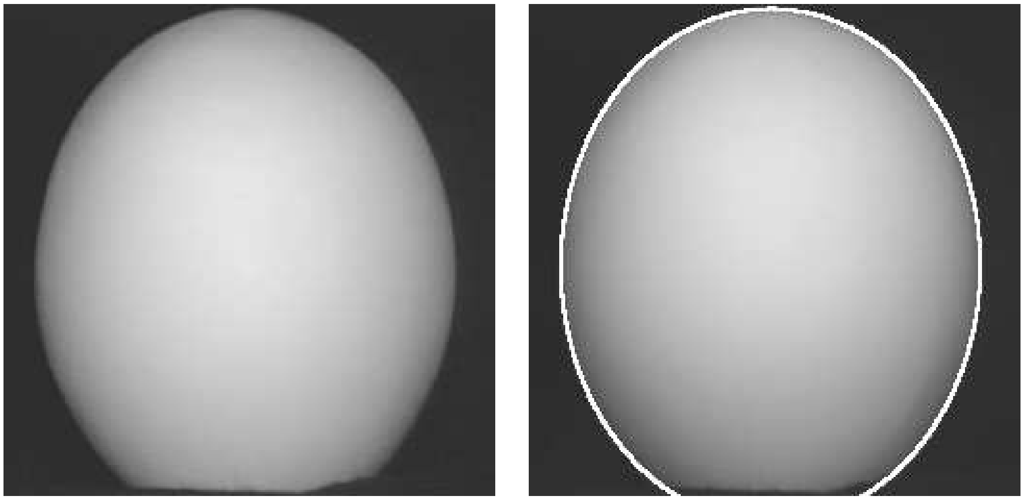

(c) Light source 3

(d) Boundary contour overlay

Figure 3: Images of calibration sphere.

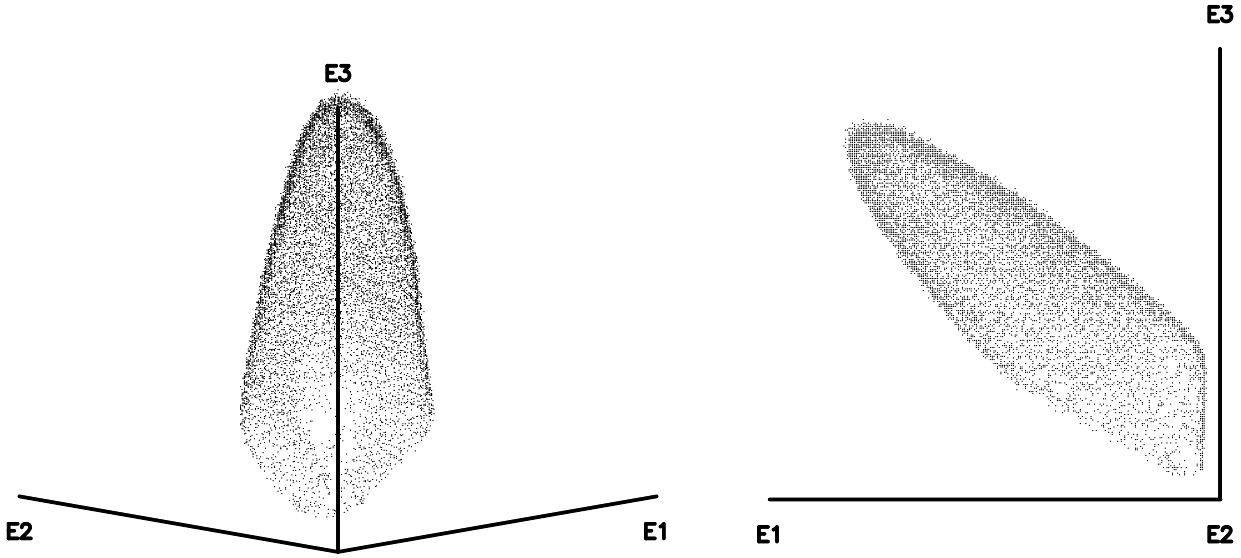

(a) elevation 10.0 azimuth 225.0

(b) elevation 0.0 azimuth 0.0

Figure 4: Calibration sphere: scatterplot of measured intensity triples.

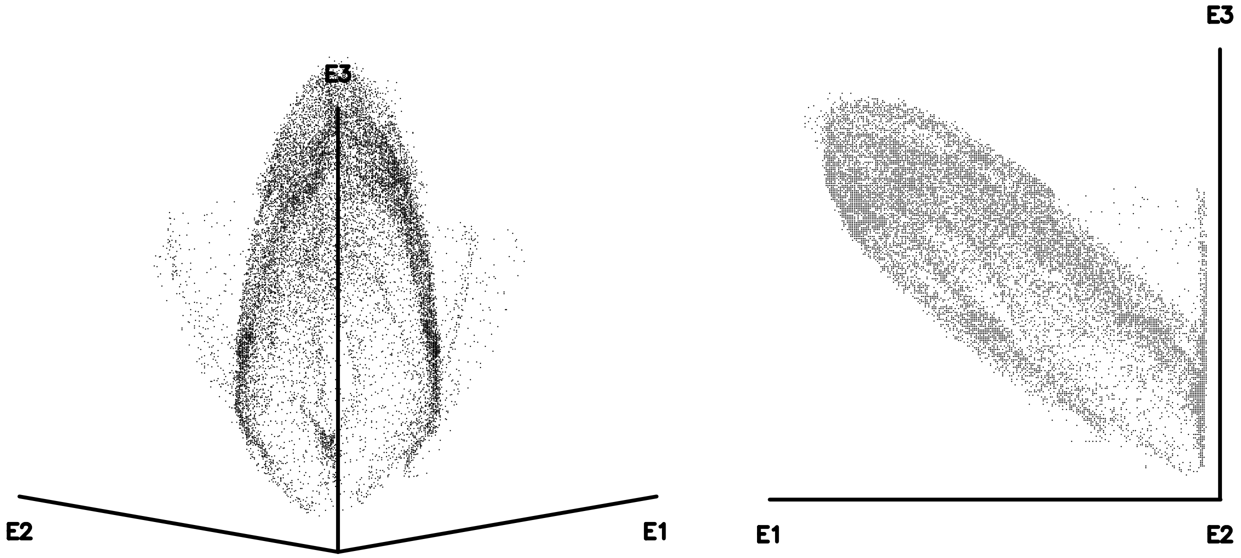

(a) elevation 10.0 azimuth 225.0

(b) elevation 0.0 azimuth 0.0

Figure 5: Doll face (frame 5): scatterplot of measured intensity triples.

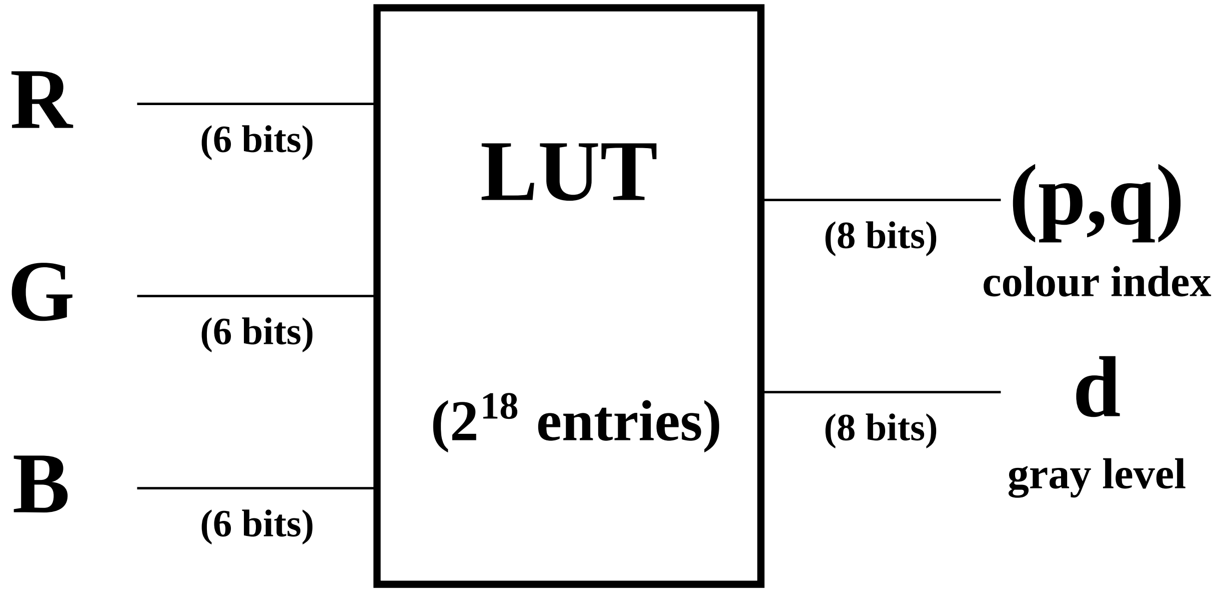

Figure 6: Lookup tables for photometric stereo. The input combines three video streams, 6 bits each for R, G and B. The output is two independent 8 bit video streams, one the colormap index for the encoding of the gradient, (p, q), and the other the gray-level encoding of distance, d, from a direct table hit. The available hardware does not have a lookup table with 2^{18} entries. Instead, the above is implemented using 4 hardware lookup tables each with 2^{16} entries.

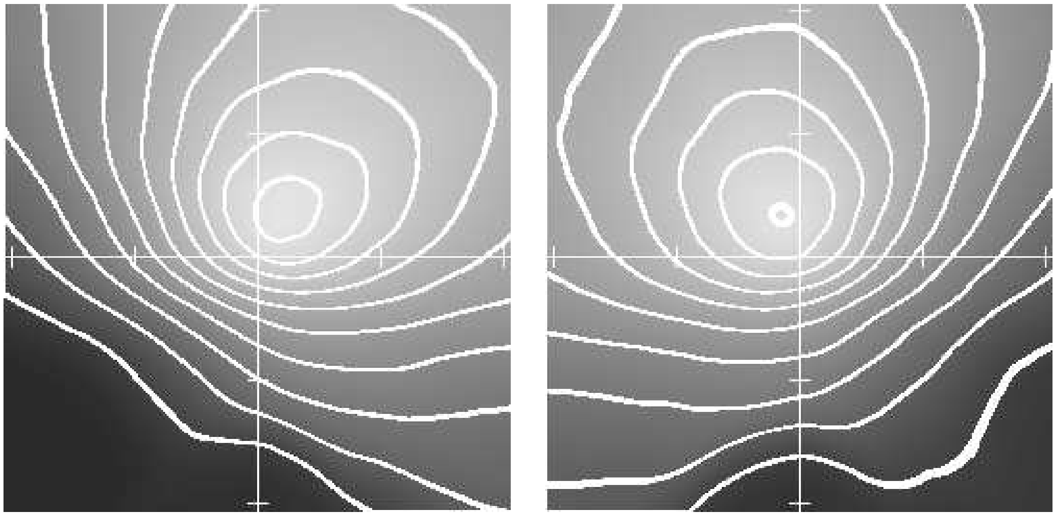

(a) Light source 1

(b) Light source 2

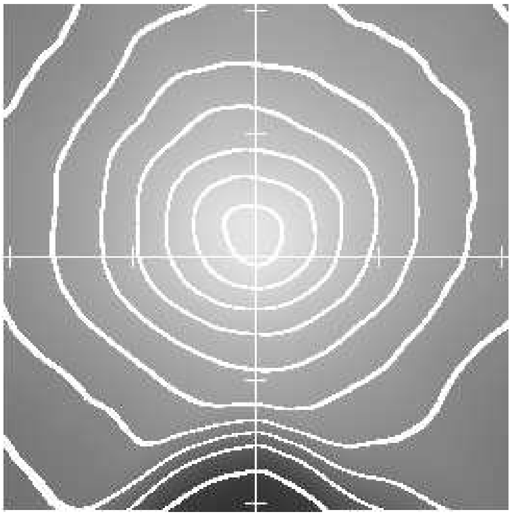

(c) Light source 3

Figure 7: The three empirically determined reflectance maps with iso-brightness contours superimposed.

(a) Light source 1

(b) Light source 2

(c) Light source 3

Figure 8: Three images of doll face (frame 5).

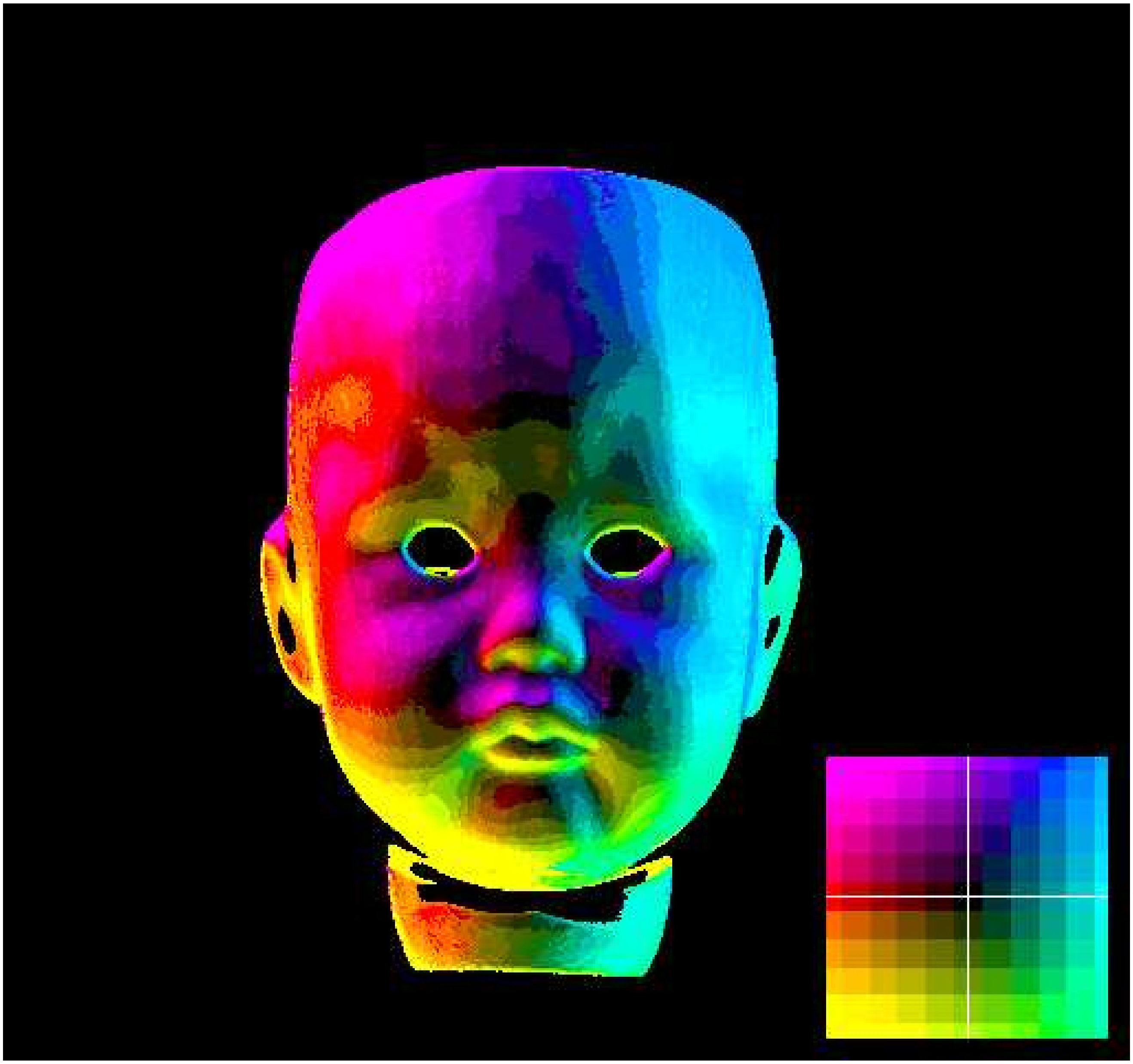

Figure 9: Example of color encoded gradient, (p, q), as produced in the near real-time (15Hz) implementation of photometric stereo. The inset (lower right) shows the color rosette used to encode the gradient.

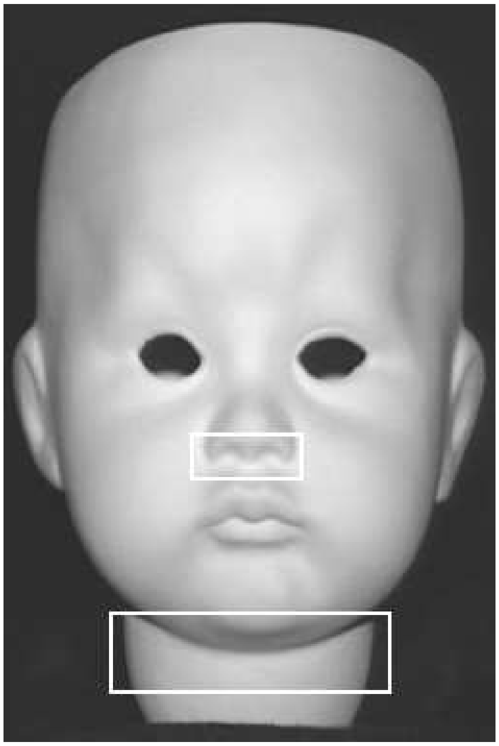

Figure 10: Selected regions from doll face (frame 5) light source 3 image. Neck region has cast shadows in the light source 1 and light source 2 images (see Figure 8(a–b)). Nostril region has significant interreflection.

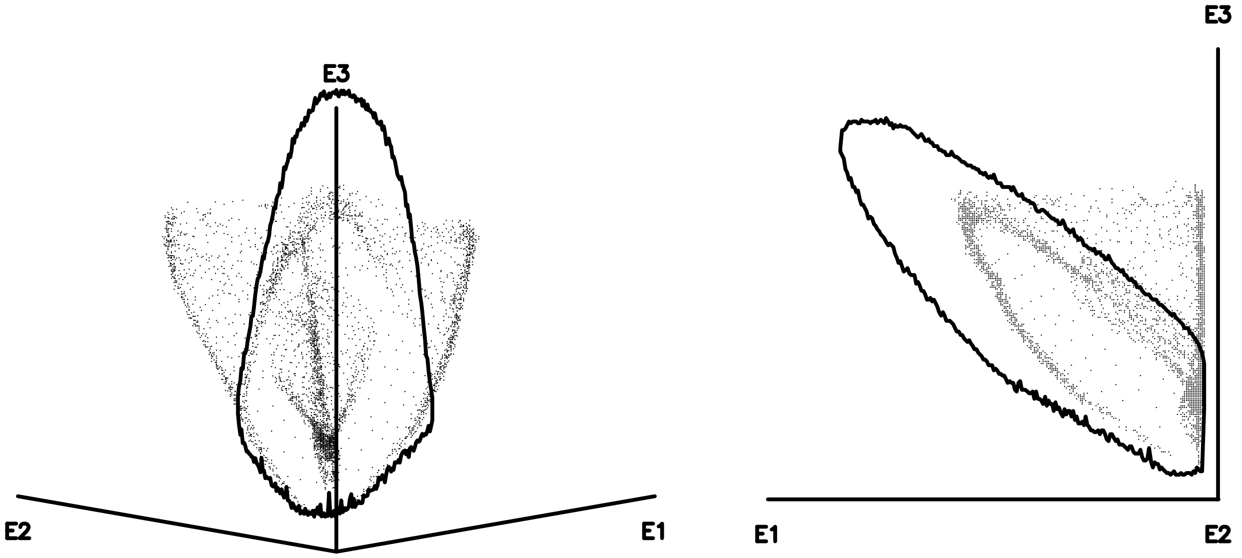

(a) elevation 10.0 azimuth 225.0

(b) elevation 0.0 azimuth 0.0

Figure 11: Doll face (frame 5): scatterplot of measured intensity triples taken from the neck region (see Figure 10) where cast shadows occur. Outline of calibration sphere scatterplot is overlayed for comparison purposes.

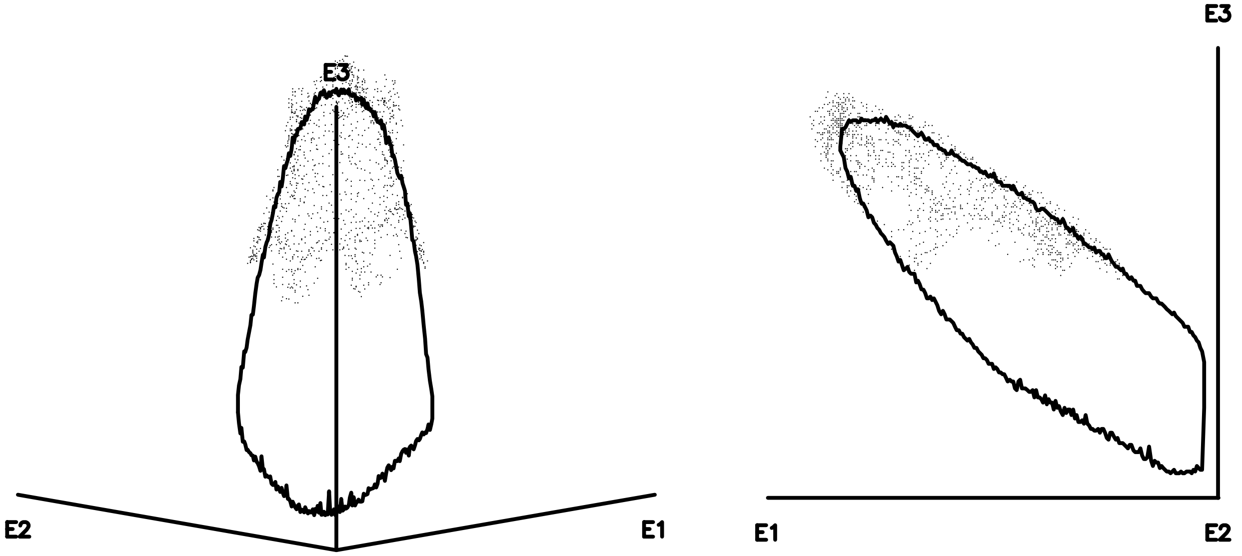

(a) elevation 10.0 azimuth 225.0

(b) elevation 0.0 azimuth 0.0

Figure 12: Doll face (frame 5): scatterplot of measured intensity triples taken from the nose region (see Figure 10) where significant interreflection occurs. Outline of calibration sphere scatterplot is overlayed for comparison purposes.

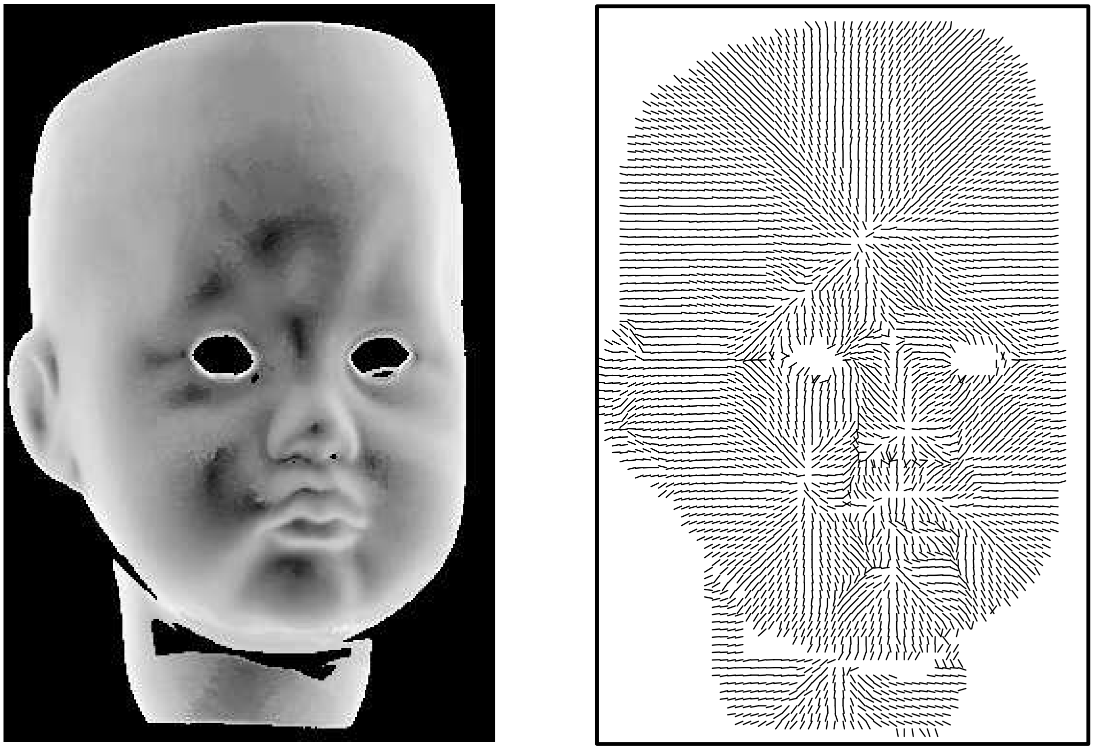

(a) Slope (frame 0) (b) Aspect (frame 0)

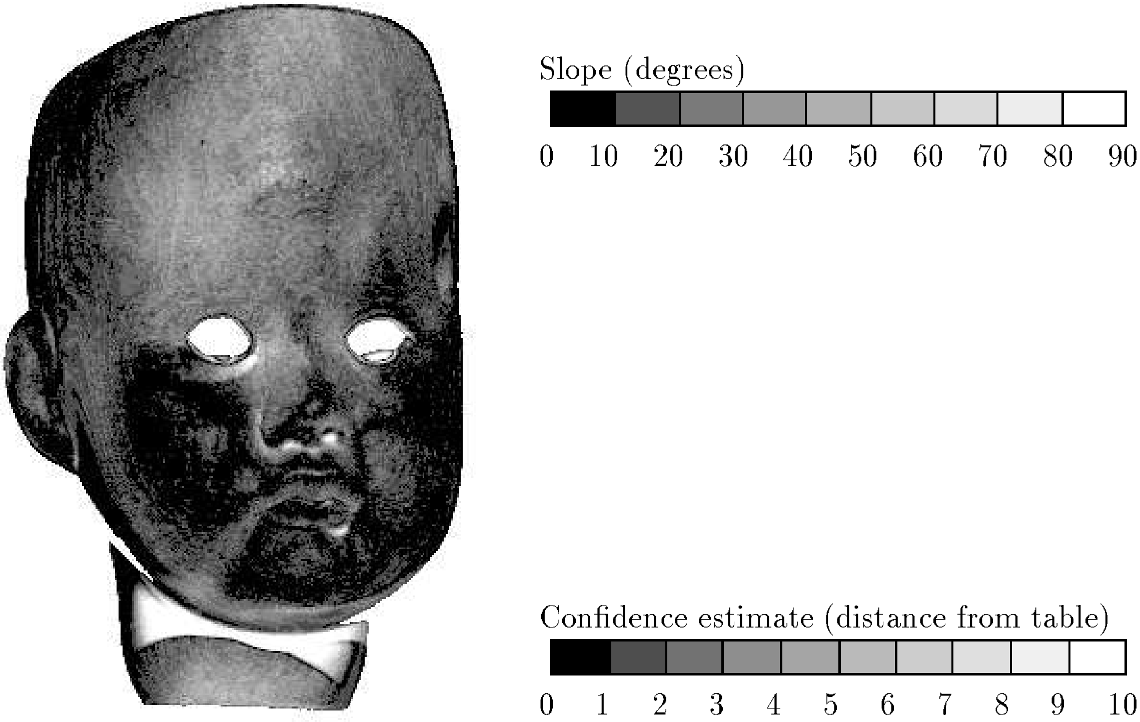

(c) Confidence Estimate (frame 0)

Figure 13: Gradient estimation for doll face (frame 0).

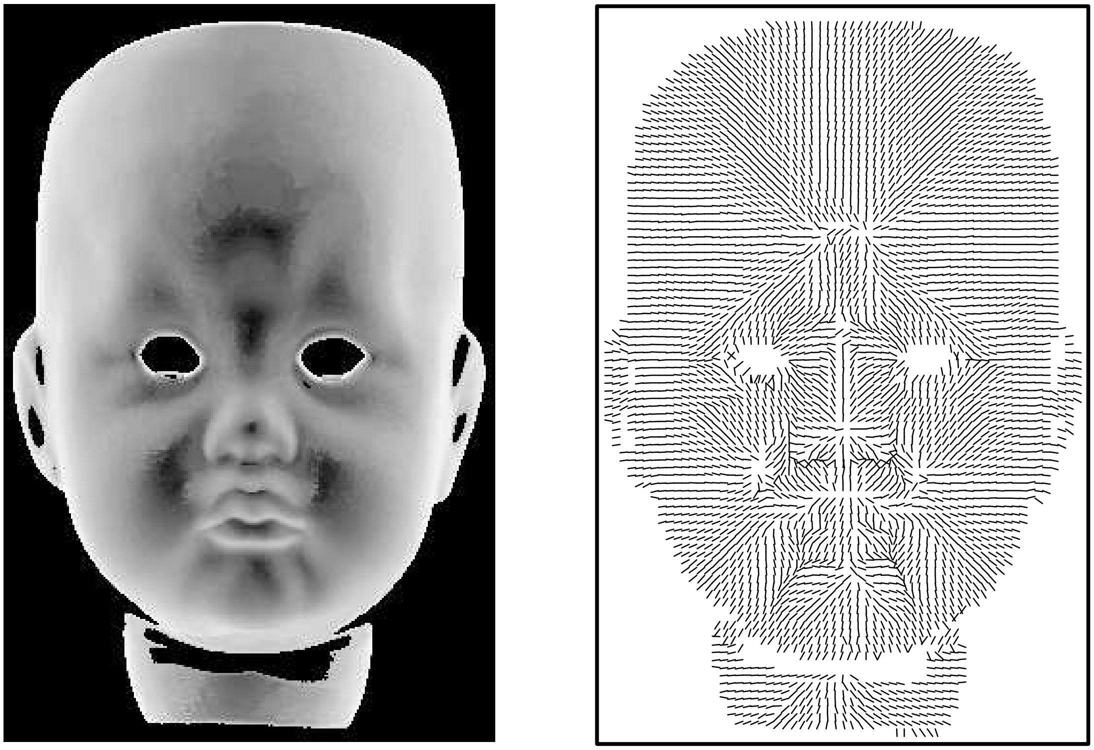

(a) Slope (frame 5)

(b) Aspect (frame 5)

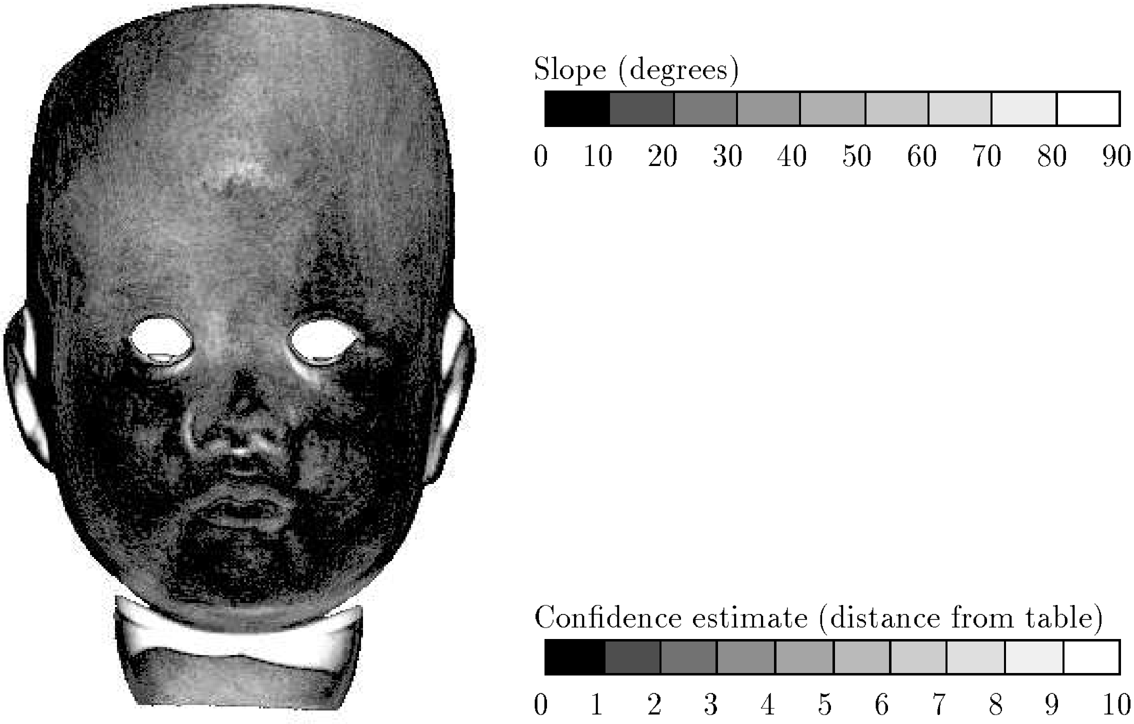

(c) Confidence Estimate (frame 5)

Figure 14: Gradient estimation for doll face (frame 5).

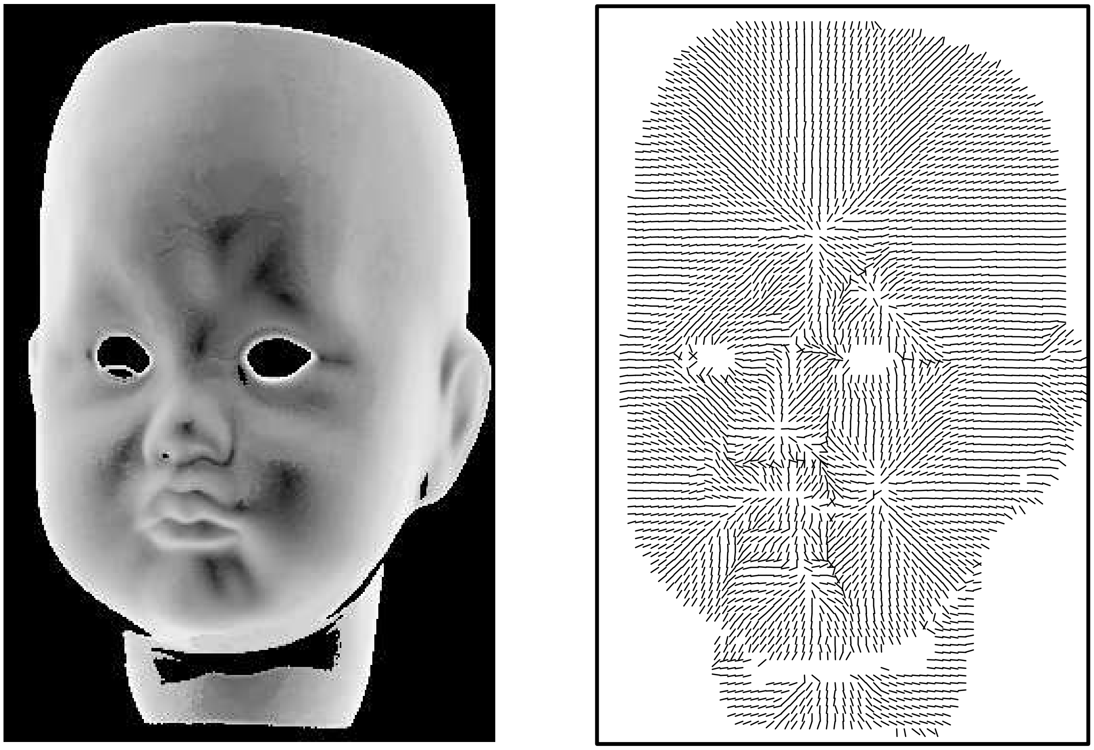

(a) Slope (frame 10)

(b) Aspect (frame 10)

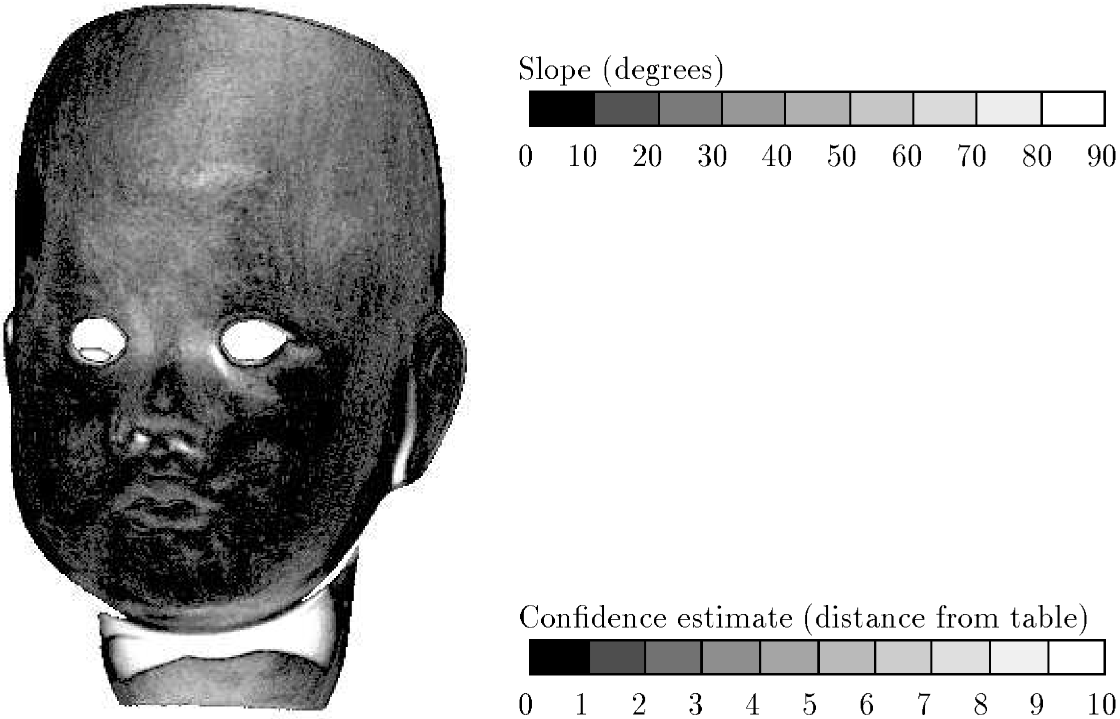

(c) Confidence Estimate (frame 10)

Figure 15: Gradient estimation for doll face (frame 10).

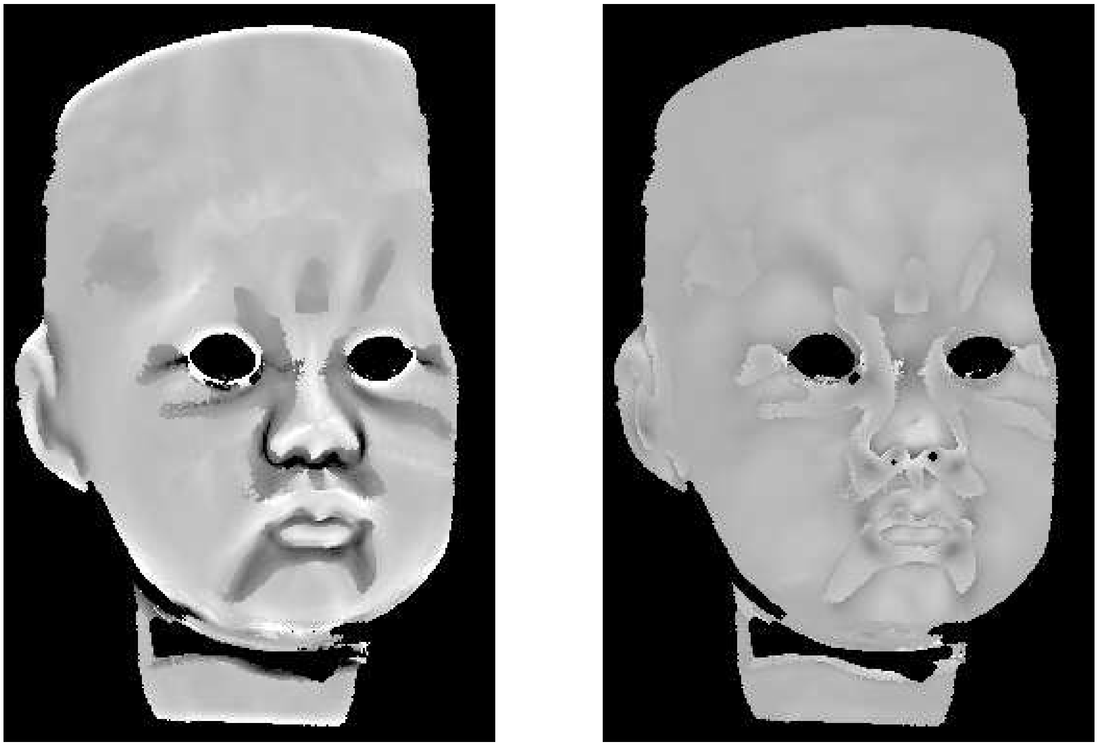

(a) Principal curvature k_1 (frame 0)

(b) Principal curvature k_2 (frame 0)

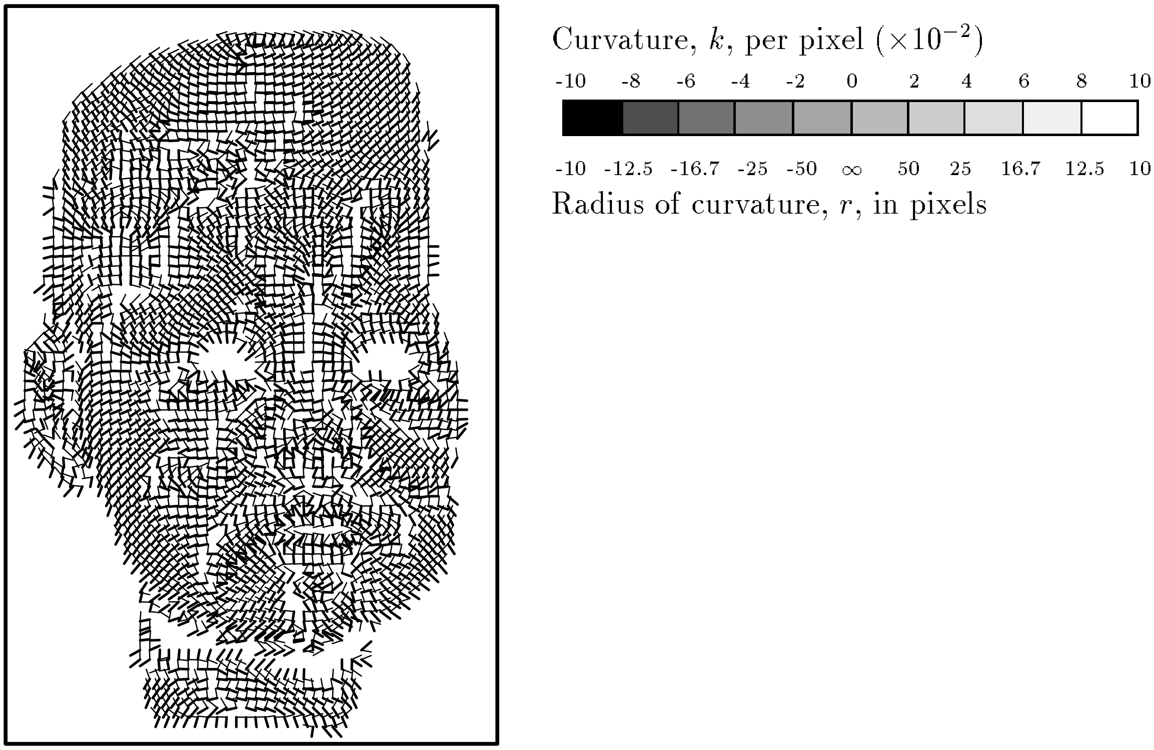

(c) Principal directions (frame 0)

Figure 16: Principal curvature estimation for doll face (frame 0).

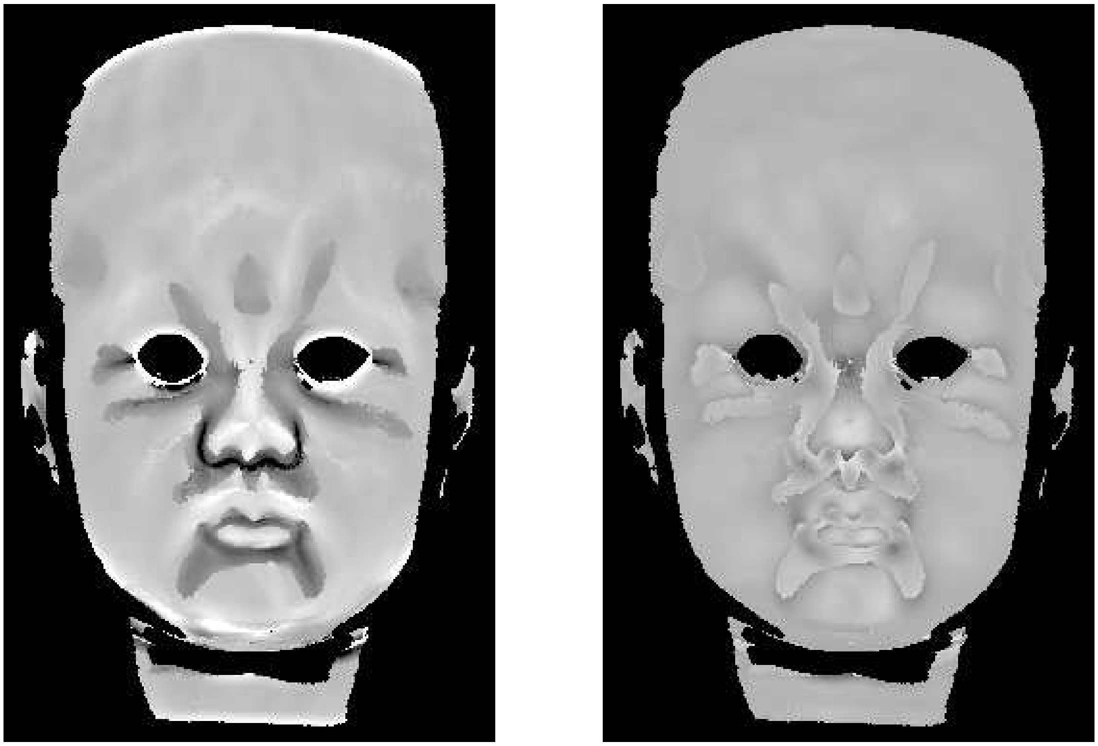

(a) Principal curvature k_1 (frame 5)

(b) Principal curvature k_2 (frame 5)

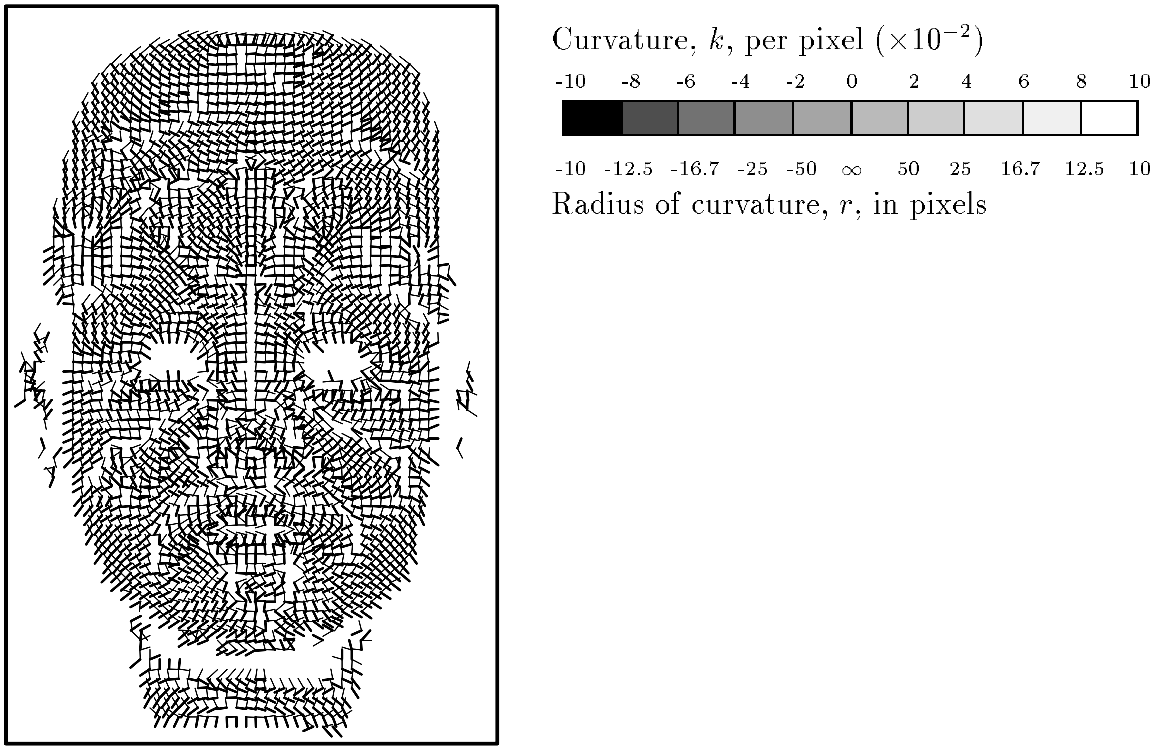

(c) Principal directions (frame 5)

Figure 17: Principal curvature estimation for doll face (frame 5).

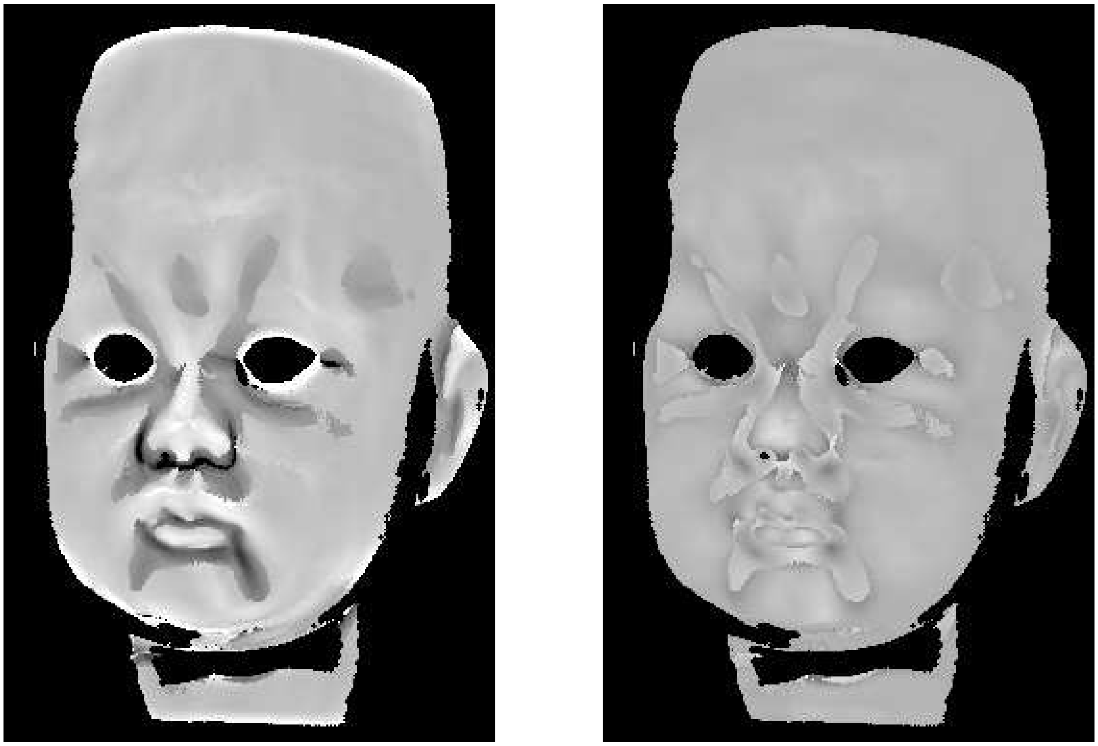

(a) Principal curvature k_1 (frame 10)

(b) Principal curvature k_2 (frame 10)

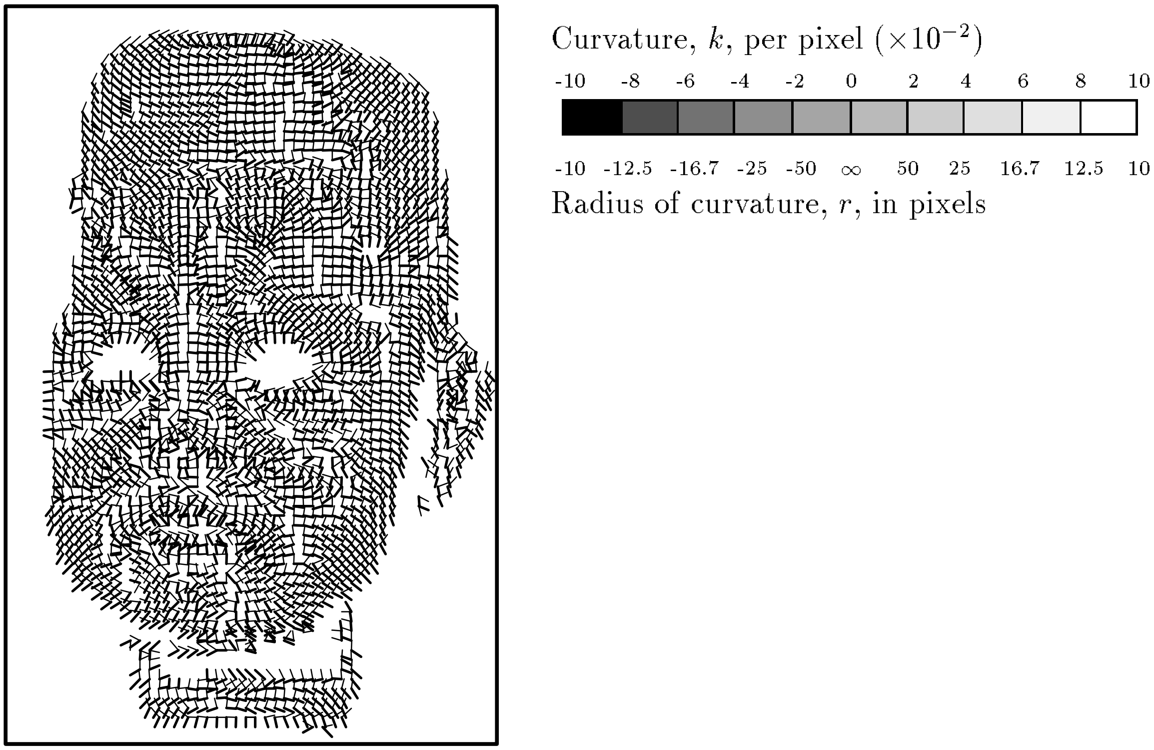

(c) Principal directions (frame 10)

Figure 18: Principal curvature estimation for doll face (frame 10).